

# MODELING UV RADIATION FEEDBACK FROM MASSIVE STARS: II. DISPERSAL OF STAR-FORMING GIANT MOLECULAR CLOUDS BY PHOTOIONIZATION AND RADIATION PRESSURE

JEONG-GYU KIM<sup>1,2</sup>, WOONG-TAE KIM<sup>1,2</sup>, & EVE C. OSTRICKER<sup>2</sup>

<sup>1</sup>Department of Physics & Astronomy, Seoul National University, Seoul 08826, Republic of Korea and

<sup>2</sup>Department of Astrophysical Sciences, Princeton University, Princeton, NJ 08544, USA

*Accepted to ApJ*

## ABSTRACT

UV radiation feedback from young massive stars plays a key role in the evolution of giant molecular clouds (GMCs) by photoevaporating and ejecting the surrounding gas. We conduct a suite of radiation hydrodynamic simulations of star cluster formation in marginally-bound, turbulent GMCs, focusing on the effects of photoionization and radiation pressure on regulating the net star formation efficiency (SFE) and cloud lifetime. We find that the net SFE depends primarily on the initial gas surface density,  $\Sigma_0$ , such that the SFE increases from 4% to 51% as  $\Sigma_0$  increases from  $13 M_\odot \text{ pc}^{-2}$  to  $1300 M_\odot \text{ pc}^{-2}$ . Cloud destruction occurs within 2–10 Myr after the onset of radiation feedback, or within 0.6–4.1 freefall times (increasing with  $\Sigma_0$ ). Photoevaporation dominates the mass loss in massive, low surface-density clouds, but because most photons are absorbed in an ionization-bounded Strömgren volume the photoevaporated gas fraction is proportional to the square root of the SFE. The measured momentum injection due to thermal and radiation pressure forces is proportional to  $\Sigma_0^{-0.74}$ , and the ejection of neutrals substantially contributes to the disruption of low-mass and/or high-surface density clouds. We present semi-analytic models for cloud dispersal mediated by photoevaporation and by dynamical mass ejection, and show that the predicted net SFE and mass loss efficiencies are consistent with the results of our numerical simulations.

*Subject headings:* H II regions — methods: numerical — ISM: clouds — ISM: kinematics and dynamics — radiation: dynamics — stars: formation

## 1. INTRODUCTION

Ultraviolet (UV) radiation produced by newborn star clusters profoundly affects the evolution of giant molecular clouds (GMCs), where most star formation in the local Universe takes place. The UV photons dissociate and ionize cold molecular gas that could otherwise fuel further star formation (e.g., Whitworth 1979). Photoionization increases the thermal pressure within GMCs by three orders of magnitude, and expansion of high-pressure ionized bubbles (H II regions) can not only mechanically unbind the parent cloud but also induce turbulent motions in the surrounding interstellar medium (ISM) (Gritschneider et al. 2009; Walch et al. 2012; Medina et al. 2014). In addition to photoionization, UV photons exert radiation pressure on dust, which is collisionally coupled to the gas. This radiation pressure force alters the internal structure of H II regions surrounding newborn luminous clusters (Draine 2011) and helps to expel the gas from GMCs. While the above processes help to quench star formation locally and globally, it has also been proposed that UV radiation can stimulate star formation either in the “collect and collapse” scenario in which swept-up shells around H II regions grow in mass and gravitationally collapse (e.g., Elmegreen & Lada 1977; Whitworth et al. 1994; Hosokawa & Inutsuka 2006; Dale et al. 2007; Deharveng et al. 2010) or via “radiation-driven implosion” in which an ionization front drives converging shock waves toward the centers of pre-existing globules (e.g., Bertoldi 1989; Sugitani et al. 1989; Lefloch & Lazareff 1994; Bisbas et al. 2011). Still,

although localized “triggering” may occur, existing simulations (see below) show that UV radiation feedback overall has a negative impact on star formation.

Compared to what would be expected from unimpeded freefall collapse, star formation in GMCs is empirically a rather slow and inefficient process (e.g., Zuckerman & Palmer 1974; Zuckerman & Evans 1974; Evans 1991). While the typical GMC freefall time is only of order  $\sim 1$ –10 Myr, the gas depletion timescale  $t_{\text{dep}}$  estimated from the ratio between gas mass and star formation rate is  $\sim 1$  Gyr for molecular gas averaged over  $\sim \text{kpc}$  scales in normal disk galaxies (e.g., Bigiel et al. 2008; Leroy et al. 2013) and somewhat shorter in galactic centers and starburst environments (e.g., Daddi et al. 2010; Leroy et al. 2015; Pereira-Santaella et al. 2016) as well as individual molecular clouds (e.g., Kennicutt & Evans 2012; Vutisalchavakul et al. 2016). In Galactic star-forming clouds, the observed star formation efficiency (SFE)—defined as the ratio of stellar to gas mass—varies widely, ranging over  $\sim 0.0001$ –0.3, and is only a few percent on average (e.g., Myers et al. 1986; Mooney & Solomon 1988; Williams & McKee 1997; Carpenter 2000; Evans et al. 2009; Murray et al. 2010; García et al. 2014; Lee et al. 2016; Vutisalchavakul et al. 2016), while evidence is accumulating that clouds in extremely dense environments may have higher SFEs (e.g., Meier et al. 2002; Turner et al. 2015; Consiglio et al. 2016; Turner et al. 2017). Yet, it is still uncertain what physical processes are responsible for the diversities in observed SFEs.

A related issue concerns the lifetime of clouds. For an idealized isolated cloud with steady star formation, the cloud lifetime  $t_{\text{cl}}$  would be related to the depletion timescale via  $t_{\text{cl}} = \varepsilon_* t_{\text{dep}}$ , where the net SFE,  $\varepsilon_*$ , is the

fraction of the initial cloud mass that will ever become stars. No consensus exists over how long an individual molecular cloud survives as a coherent entity (Heyer & Dame 2015). On the one hand, it has been argued that the short age spreads ( $\lesssim 5$  Myr) of stellar populations in nearby star-forming clouds supports the picture that star-forming clouds are dispersed rapidly—on the cloud’s dynamical timescale (e.g. Hartmann 2001; Hartmann et al. 2001, but see also Da Rio et al. 2014, who argue that cluster formation takes several local dynamical timescales). On the other hand, estimates based on the fraction of GMCs that are spatially coincident with H II regions and young star clusters in nearby galaxies favor lifetimes of a few tens of Myrs (Engargiola et al. 2003; Blitz et al. 2007; Kawamura et al. 2009; Miura et al. 2012; see also Murray 2011; Meidt et al. 2015; Lee et al. 2016). The cloud lifetime also has implications for the origin and maintenance of turbulence in GMCs. While supersonic turbulence appears to be pervasive in GMCs (Elmegreen & Scalo 2004), its energy begins to decay within one large-scale crossing time in the absence of driving (e.g., Mac Low et al. 1998; Stone et al. 1998). If GMCs are very long lived, turbulence must be driven continuously (but not excessively) by internal or external processes to support them against gravitational collapse without dispersal (Krumholz et al. 2006; Goldbaum et al. 2011), while this kind of finely calibrated turbulent driving is not needed if GMCs are dispersed rapidly (Elmegreen 2000; Ballesteros-Paredes 2006; Ballesteros-Paredes et al. 2011).

A number of theoretical studies have invoked the destructive role of UV radiation feedback to explain the observed SFEs and lifetimes of GMCs (see reviews by McKee & Ostriker 2007; Krumholz et al. 2014). Analytic models based on idealized solutions for expanding blister-type H II regions found that the net SFE of  $\varepsilon_* \sim 5\text{--}15\%$  is sufficient to disperse typical GMCs in the Milky Way (mass  $M \sim 10^5\text{--}10^6 M_\odot$  and surface density  $\Sigma \sim 10^2 M_\odot \text{pc}^{-2}$ ) by photoevaporation and dynamical disruption in a few tens of Myr (Whitworth 1979; Williams & McKee 1997; Matzner 2002; Krumholz et al. 2006). Krumholz & Matzner (2009), Fall et al. (2010), and Murray et al. (2010) highlighted the importance of radiation pressure on dust grains in controlling the dynamics of H II regions in dense, massive star-forming environments. Kim et al. (2016) studied dynamical disruption of clouds by considering the expansion of a swept-up spherical shell surrounding a central H II region, and found that the minimum SFE required for cloud disruption increases primarily with the cloud’s surface density and that the disruption timescale is comparable to the freefall time. These models also suggest that radiation pressure is expected to be more important than ionized-gas pressure in massive and high surface density clouds (see also Krumholz & Matzner 2009; Fall et al. 2010). More recently, Rahner et al. (2017) developed a semi-analytic model for the dynamics of an expanding shell formed around a star cluster including the effects of radiation pressure, stellar winds, and supernovae (SNe) (but not including effects of ionized-gas pressure), and evaluated the minimum SFE as well as the relative importance of each feedback mechanism.

While analytic approaches offer valuable insights into

the physical processes involved in cloud dispersal, they are limited to smooth and/or spherically symmetric density distributions. Real GMCs are turbulent and extremely inhomogeneous. As a consequence, shell expansion induced by H II regions from multiple subclusters is not spherically symmetric, and neither embedded nor blister H II regions present smooth interior surfaces to photoionizing radiation. To quantitatively follow the formation and evolution of multiple cluster-containing H II regions in highly turbulent, inhomogeneous clouds, and to quantitatively assess the consequences of the complex interplay between gas and UV radiation, numerical radiation hydrodynamic (RHD) simulations are necessary (see recent reviews by Krumholz et al. 2014; Dale 2015).

Several numerical studies have investigated the effects of photoionization feedback on dynamical evolution of GMCs. For instance, Vázquez-Semadeni et al. (2010) and Colín et al. (2013) allowed for photoheating by ionizing radiation in the evolution of GMCs produced by colliding flows and showed that the feedback reduces SFEs significantly. Using smoothed particle hydrodynamics simulations, Dale et al. (2012, 2013) performed RHD simulations of star cluster formation in turbulent GMCs over a 3 Myr timescale before the first supernova event occurs. Their parameter study showed that while photoionization can unbind a significant fraction of material in low-mass, diffuse clouds, it has a limited impact for clouds with escape velocities larger than the sound speed of ionized gas. Gavagnin et al. (2017) studied the early (2 Myr) dynamical evolution of a star cluster formed in a turbulent cloud with mass  $2.5 \times 10^4 M_\odot$  and surface density  $250 M_\odot \text{pc}^{-2}$  and found that photoionization can limit the net SFE to 20%. Geen et al. (2017) performed RHD simulations of magnetized,  $10^4 M_\odot$ -mass clouds of varying size and found that the net SFE increases from 0.04 to 0.6 as the surface density increases from 14 to  $1100 M_\odot \text{pc}^{-2}$ .

Considering the effects of non-ionizing UV, Raskutti et al. (2016) conducted RHD simulations of cluster-forming turbulent clouds, focusing exclusively on the radiation pressure from singly-scattered, non-ionizing UV. They found that the resulting net SFE ( $\varepsilon_* \sim 0.1\text{--}0.6$  for  $\Sigma \sim 10\text{--}300 M_\odot \text{pc}^{-2}$ ) in turbulent cloud simulations is much higher than that expected for the case of a uniform shell. This is because turbulent shock compression leads to a broad (log-normal) distribution of the gas surface density, which in turn increases the fraction of super-Eddington, high surface-density gas that is difficult to unbind and hence subject to star formation (see also Thompson & Krumholz 2016). Raskutti et al. (2016) concluded that feedback from radiation pressure alone is unable to explain the low SFEs of observed GMCs.

More recently, Howard et al. (2017) performed a series of RHD simulations to study the early phase ( $\lesssim 5$  Myr) of GMC evolution, including both photoionization and radiation pressure. They considered a set of GMC models with the same mean density ( $n_H \sim 150 \text{cm}^{-3}$ ) but differing mass ( $10^4\text{--}10^6 M_\odot$ ), and found a modest degree of suppression in the SFE compared to the runs in which they turned off radiation feedback. In their models, the impact of radiative feedback varied without a clear trend with the cloud mass; only intermediate-mass clouds ( $5 \times 10^4 M_\odot$  and  $10^5 M_\odot$ ) were fully ionized and

destroyed in 5 Myr.

While the above numerical studies have improved our understanding of the effects of UV radiation on GMC evolution and star formation regulation, several important issues still need to be addressed. First, although several studies have emphasized the importance of photoionization and radiation pressure for cloud dispersal, as yet there is no systematic accounting that quantifies to what extent each mechanism, alone and combined, is responsible for the net SFE and cloud disruption. Second, most of the previous simulations have only used approximate methods for treating the radiative transfer problem for multiple point sources. For example, Vázquez-Semadeni et al. (2010) incorporated photoionization feedback by depositing thermal energy to a gas cell where a stellar particle resides. Dale et al. (2012, 2013) adopted the “Strömgren volume technique” to calculate the ionization state of gas, but did not consider the effects of radiation pressure on dust. Simulations by Raskutti et al. (2016, 2017), Gavagnin et al. (2017), and Geen et al. (2017) adopted two-moment methods to evolve the radiation energy and momentum on a grid with the  $M_1$ -closure. Although the  $M_1$ -closure is accurate for a spatially concentrated source distribution, it becomes less accurate when multiple point sources are widely distributed; this method also has inherently limited resolution in the immediate vicinity of point sources (see Kim et al. 2017, hereafter Paper I). Thus, a firm quantitative assessment of the importance of both photoionization and radiation pressure on cloud dispersal requires a more accurate solution of the radiative transfer equation than has previously been available.

In this work, we have carried out RHD simulations of star cluster formation in turbulent clouds employing the adaptive ray tracing method (Abel & Wandelt 2002), which enables us to accurately solve the radiative transfer problem for multiple point sources and both ionizing and non-ionizing radiation. In Paper I we described our implementation and tests of adaptive ray tracing in the *Athena* magnetohydrodynamics code (Stone & Gardiner 2009), for which we adopted the novel parallelization algorithm proposed by Rosen et al. (2017) as well as several other improvements. The excellent parallel performance this has enabled for ray tracing allows us to run a large number of simulations, probing a range of cloud masses and sizes efficiently. In the present paper, our primary goals are (1) to quantify the dependence on the cloud properties of the net SFE, timescale for cloud disruption, mass of ionized outflows, and momentum transferred to gas outflows, and (2) to assess the relative importance of photoionization and radiation pressure in various environments. In addition, we develop analytic predictions for mass loss based on the physical scalings for photoevaporation and momentum injection, and we compare the predictions for the net SFE with the numerical results.

The organization of this paper is as follows. Section 2 presents the numerical methods and cloud parameters that we adopt. Section 3 first describes the overall evolution of our fiducial model, and then explores the parameter dependence of various integrated physical quantities for different models. In Section 4, we present a detailed analysis of the mass loss caused by photoevaporation and momentum injection. In Section 5, we construct

the semi-analytic models for the net SFE and mass loss efficiencies of GMCs regulated by UV radiation feedback, and compare the model predictions with the numerical results. In Section 6, we summarize and discuss the astronomical implications of our results. In Appendix A, we present the results of convergence study for the fiducial model. In Appendix B, we compare our numerical results for SFE in radiation-pressure only models to analytic predictions.

## 2. NUMERICAL METHODS

For our numerical simulations, we use the Eulerian grid-based code *Athena* (Stone et al. 2008) equipped with additional physics modules for self-gravity, sink particles, and radiative transfer from point sources. In Paper I, we presented a detailed description of our implementation of the adaptive ray tracing algorithm for multiple point sources in *Athena*, including parallelization and the methods for solving photoionization and recombination. Paper I also described the initial conditions and problem setup for our simulations of cluster-forming turbulent clouds. Below we briefly summarize the highlights of our numerical methods and describe the initial cloud parameters.

### 2.1. Radiation Hydrodynamics Scheme

For hydrodynamics, we employ *Athena*’s van Leer-type time integrator (Stone & Gardiner 2009), the HLLC Riemann solver, and a piecewise linear spatial reconstruction scheme. We use the fast Fourier transformation Poisson solver with open boundary conditions (Skinner & Ostriker 2015) to calculate the gravitational forces from gas and stars; the stellar contribution is handled with the particle-mesh method using the triangular-shaped-cloud interpolation scheme (Hockney & Eastwood 1981).

We apply the sink particle technique of Gong & Ostriker (2013) to model the formation and growth of star clusters. We create a star particle if a cell with density above the Larson-Penston threshold density ( $\rho_{\text{crit}} \equiv 8.86 c_{\text{s,neu}}^2 / (\pi G \Delta x^2)$ ) for the sound speed of neutral gas  $c_{\text{s,neu}}$  and the grid spacing  $\Delta x$ ) has a converging velocity field and corresponds to the local minimum of the gravitational potential. The accretion rates of mass and momentum onto each sink are computed from the flux through the surfaces of the  $3^3$ -cell control volume centered at the sink particle; this control volume acts like internal ghost zones within the simulation domain. The positions and velocities of sink particles are updated using a leapfrog integrator. We allow sink particles to merge if their control volumes overlap.

Due to limited resolution, the sink particles in our simulations represent subclusters rather than individual stars<sup>1</sup>, and may not fully sample the initial mass function. Using the mass-dependent light-to-mass ratios from Kim et al. (2016), we determine the total UV luminosity of cluster particles for two frequency bins,  $L_i$  and  $L_n$ , representing Lyman continuum photons and far-UV photons, such as  $L \equiv L_i + L_n =$

<sup>1</sup> The typical mass of newly formed sink particles is  $M_{\text{sink}} \sim 10 \rho_{\text{crit}} \Delta x^3 \approx 240 M_{\odot} (R_0/20 \text{ pc}) (N_x/256)^{-1}$ , where  $\rho_{\text{crit}}$  is the threshold for sink particle creation,  $R_0$  is the initial cloud radius, and  $N_x$  is the number of grid zones in the domain in one direction.



$\Psi M_*$  and  $Q_i \equiv L_i/(h\nu_i) = \Xi M_*$ , where  $M_*$  is the total cluster mass,  $\Psi = 10^{2.98\mathcal{X}^6/(29.0+\mathcal{X}^6)} L_\odot M_\odot^{-1}$ ,  $\Xi = 10^{46.7\mathcal{X}^7/(7.28+\mathcal{X}^7)} \text{s}^{-1} M_\odot^{-1}$  with  $\mathcal{X} = \log_{10}(M_*/M_\odot)$ , and  $h\nu_i = 18 \text{ eV}$  is the mean energy of ionizing photons. Note that  $\Psi \simeq 943 L_\odot M_\odot^{-1}$  and  $\Xi \simeq 5.05 \times 10^{46} \text{s}^{-1} M_\odot^{-1}$  are almost constant for  $M_* \gtrsim 10^3 M_\odot$ , while varying steeply for  $M_* < 10^3 M_\odot$  (see Figure 14 of Kim et al. 2016). The luminosity of individual cluster particles are assumed to be proportional to their mass. The use of mass-dependent conversion factors approximately captures the effect of undersampling at the massive end of the initial mass function when the total cluster mass is below  $\sim 10^3 M_\odot$ .

In the present paper, we do not consider evolution of the stellar light-to-mass ratio. The UV luminosity of a coeval stellar population that well samples the initial mass function remains approximately constant for the main sequence lifetime of the most massive star, implying that ionizing and non-ionizing luminosities would in practice decay rapidly after timescales of 3 Myr and 8 Myr, respectively (e.g., Parravano et al. 2003). Caveats related to our adoption of age-independent luminosity are discussed in Section 6.2.

The radiative transfer of ionizing and non-ionizing photons is handled by the adaptive ray tracing method (Abel & Wandelt 2002). For each radiating star particle, we generate  $12 \times 4^4 = 3072$  initial rays and allow photon packets to propagate radially outward, computing the cell-ray intersection length and the corresponding optical depth on a cell-by-cell basis. The volume-averaged radiation energy and flux densities of a cell are computed from the sum of the contributions from all rays that pass through the cell (see Section 2.1 of Paper I). These averages are used to compute the radiation force from the combined non-ionizing and ionizing radiation fields, and the ionization rate of neutral gas. Because the fluid variables and gravity in the  $3^3$  cells surrounding each sink/source particle are unresolved, we do not allow photon packets to interact with the gas within these control volumes. The radiation field directions are angularly well resolved, and the rays contain all of the photon packets from each source, when they emerge from the control volume around each source particle. This eliminates the potential problem of momentum cancellation caused by volume-averaging in the cell containing a source, noted recently by Hopkins & Grudić (2018), without the need to introduce assumptions regarding the sub-cell distributions of gas density, gravity, or the radiation field within individual zones that contain sink/source particles.

The rays are discretized and split based on the HEALPix framework (Górski et al. 2005), ensuring that each grid cell is sampled by at least four rays per source. We rotate ray propagation directions randomly at every hydrodynamic time step to reduce the numerical errors due to angle discretizations (Krumholz et al. 2007). For simplicity, we use constant photoionization cross-section for neutral hydrogen atom  $\sigma_{\text{H}^0} = 6.3 \times 10^{-18} \text{ cm}^2$  (Krumholz et al. 2007)<sup>2</sup> and constant dust absorption

(and pressure) cross-section per H nucleon  $\sigma_d = 1.17 \times 10^{-21} \text{ cm}^2 \text{ H}^{-1}$  both for ionizing and non-ionizing radiation (e.g., Draine 2011). We determine the degree of hydrogen ionization by solving the time-dependent rate equation for hydrogen photoionization and recombination (under the on-the-spot approximation). The ray-trace and ionization update are subcycled relative to the hydrodynamic update. The timestep size for each sub-step is determined to ensure that the maximum change in the neutral fraction  $x_n = n_{\text{H}^0}/n_{\text{H}}$  is less than 0.1. The source term updates for the ionization fraction and radiative force are explicit and performed at every sub-step in an operator-split fashion. The gas temperature is set to vary according to  $x_n$  between  $T_{\text{neu}} = 20 \text{ K}$  and  $T_{\text{ion}} = 8000 \text{ K}$ , the temperature of the fully neutral and ionized gas, respectively. The corresponding isothermal sound speeds are  $c_{s,\text{neu}} = 0.26 \text{ km s}^{-1}$  and  $c_{s,\text{ion}} = 10.0 \text{ km s}^{-1}$ .

We note that determining gas temperature solely based on the neutral fraction, together with adoption of constant cross-sections for photoionization and dust absorption, will certainly simplify temperature distributions inside H II regions compared to what would be more complex in realistic environments. To properly model ionization and temperature structure, as well as small-scale dynamical instabilities of ionization fronts that may operate (e.g., Kim & Kim 2014; Baczynski 2015), one has to accurately solve the energy equation after considering various cooling and heating processes as well as the frequency dependence of the cross-sections.

## 2.2. Initial and Boundary Conditions

Our initialization and boundary treatment are the same as in Skinner & Ostriker (2015) and Raskutti et al. (2016). The initial conditions for each model consist of an isolated, uniform-density sphere of neutral gas with mass  $M_0$  and radius  $R_0$  surrounded by a tenuous external medium situated in a cubic box with sides  $L_{\text{box}} = 4R_0$ .<sup>3</sup> The cloud is initially supplied with turbulent energy with velocity power  $|\delta \mathbf{v}_k|^2 \propto k^{-4}$  for  $2 \leq kL_{\text{box}}/(2\pi) \leq 64$  and zero power otherwise. We adjust the amplitude of the velocity perturbations to make the cloud marginally bound gravitationally, with the initial virial parameter of  $\alpha_{\text{vir},0} = 5\sigma_0^2 R_0/(3GM_0) = 2$ , where  $\sigma_0$  denotes the initial (three-dimensional) velocity dispersion. There is no subsequent artificial turbulent driving. The standard resolution for the simulation domain is  $N_{\text{cell}} = 256^3$  cells.

We apply diode-like outflow boundary conditions both at the boundaries of the simulation box and at the boundary faces of the control volume of each sink particle. The diode-like conditions allow mass and momentum to flow into ghost zones but not out from it. When sink particles accrete while moving across grid zones, we ensure that the total mass and momentum of gas and stars are conserved by taking into account differences in the mass and momentum of cells entering and leaving the control volume. Over the course of evolution, we separately monitor the mass outflow rates of neutral and

smaller  $\sigma_{\text{H}^0}$  can increase the neutral fraction of ionized gas inside the H II region, we have checked that it has little impact on the simulation outcome.

<sup>3</sup> Including the tenuous external medium, the initial gas mass in our simulation domain is  $1.015M_0$ .

<sup>2</sup> Our adopted photoionization cross-section corresponds to the value at the Lyman edge. The frequency-averaged cross-section depends on the local radiation spectrum and is typically smaller by a factor of  $\sim 2$  (e.g., Baczynski et al. 2015). Although the use of

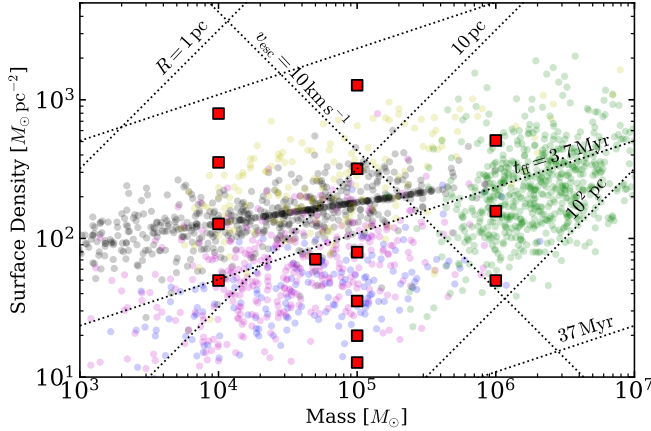


FIG. 1.— Locations of our model clouds (red squares) in the  $M$ – $\Sigma$  plane. Other symbols denote the observed molecular clouds in the literature:  $^{13}\text{CO}$  Galactic Ring Survey from Heyer et al. (2009) (blue) and Roman-Duval et al. (2010) (black),  $^{12}\text{CO}$  survey of Galactic Center Oka et al. (2001) (yellow),  $^{12}\text{CO}$  survey of Large Magellanic Clouds from Wong et al. (2011) (magenta), and  $^{12}\text{CO}$  survey of M51 from Colombo et al. (2014) (green). Dotted lines draw the loci of constant radius, escape velocity, and freefall time. ionized gas from the computational domain, as well as escape fractions of ionizing and non-ionizing photons.

### 2.3. Models

Our aim is to explore the effects of radiation feedback on cloud dispersal across a range of cloud masses and sizes, corresponding to GMCs observed in the Milky Way and nearby galaxies. These clouds are usually optically thick to UV radiation ( $\Sigma \gtrsim \kappa_{\text{UV}}^{-1} \sim 10^1 M_\odot \text{pc}^{-2}$ ) but transparent to dust-reprocessed infrared radiation ( $\Sigma \lesssim \kappa_{\text{IR}}^{-1} \sim 10^3 M_\odot \text{pc}^{-2}$ ). The momentum deposition by multiple scatterings of infrared photons may play an important role in the dynamics of extremely dense and massive clouds, such as the progenitors of super star clusters, in dust-rich environments (e.g., Skinner & Ostriker 2015; Tsang & Milosavljevic 2017).

We consider 14 clouds with  $M_0$  in the range of  $10^4 M_\odot$  to  $10^6 M_\odot$  and  $R_0$  from 2 pc to 80 pc: the resulting initial surface density  $\Sigma_0 = M_0/(\pi R_0^2)$  is in the range from  $12.7 M_\odot \text{pc}^{-2}$  to  $1.27 \times 10^3 M_\odot \text{pc}^{-2}$ . Figure 1 plots the locations (red squares) of our model clouds in the  $M$ – $\Sigma$  domain, compared to observed GMCs (circles) compiled from the literature (note that a range of different methods have been adopted in the literature to estimate observed cloud surface density and mass). Table 1 lists the initial physical parameters of our model clouds. Column 1 gives the name of each model. Columns 2–4 list  $M_0$ ,  $R_0$ , and  $\Sigma_0$ , respectively. Columns 5 and 6 give the number density of hydrogen atoms  $n_{\text{H},0}$  and the freefall time  $t_{\text{ff},0} = \sqrt{3\pi/(32G\rho_0)}$ . Finally, Column 7 gives the escape velocity  $v_{\text{esc},0} = \sqrt{2GM_0/R_0}$  at the cloud surface. The initial turbulent velocity dispersion in each cloud is  $\sigma_0 = 0.77v_{\text{esc},0}$ . We take model M1E5R20 with  $M_0 = 10^5 M_\odot$ ,  $R_0 = 20 \text{ pc}$ , and  $t_{\text{ff},0} = 4.7 \text{ Myr}$  as our fiducial model, which is typical of Galactic GMCs and comparable in mass and size to the Orion A molecular cloud (e.g., Wilson et al. 2005).

TABLE 1  
MODEL CLOUD PARAMETERS

Model (1)	$M_0$ (2)	$R_0$ (3)	$\Sigma_0$ (4)	$n_{\text{H},0}$ (5)	$t_{\text{ff},0}$ (6)	$v_{\text{esc},0}$ (7)
M1E5R50	$1 \times 10^5$	50.0	12.7	5.5	18.5	4.1
M1E5R40	$1 \times 10^5$	40.0	19.9	10.8	13.2	4.6
M1E5R30	$1 \times 10^5$	30.0	35.4	25.5	8.6	5.4
M1E4R08	$1 \times 10^4$	8.0	49.7	134.7	3.7	3.3
M1E6R80	$1 \times 10^6$	80.0	49.7	13.5	11.8	10.4
M5E4R15	$5 \times 10^4$	15.0	70.7	102.2	4.3	5.4
<b>M1E5R20</b>	<b><math>1 \times 10^5</math></b>	<b>20.0</b>	<b>79.6</b>	<b>86.2</b>	<b>4.7</b>	<b>6.6</b>
M1E4R05	$1 \times 10^4$	5.0	127.3	551.8	1.9	4.1
M1E6R45	$1 \times 10^6$	45.0	157.2	75.7	5.0	13.8
M1E5R10	$1 \times 10^5$	10.0	318.3	689.7	1.7	9.3
M1E4R03	$1 \times 10^4$	3.0	353.7	2554.6	0.9	5.4
M1E6R25	$1 \times 10^6$	25.0	509.3	441.4	2.1	18.6
M1E4R02	$1 \times 10^4$	2.0	795.8	8621.6	0.5	6.6
M1E5R05	$1 \times 10^5$	5.0	1273.2	5517.8	0.6	13.1

NOTE. — Parameters listed are for initial conditions of spherical clouds. Column 1: model name. Column 2: cloud mass ( $M_\odot$ ). Column 3: cloud radius (pc). Column 4: gas surface density ( $M_\odot \text{pc}^{-2}$ ). Column 5: number density of neutral gas ( $\text{cm}^{-3}$ ). Column 6: freefall time (Myr). Column 7: escape velocity at the cloud surface ( $\text{km s}^{-1}$ ). The fiducial model M1E5R20 is shown in bold.

In addition to the standard runs including both photoionization and radiation pressure (PH+RP), we run two control simulations for each cloud, in which either only photoionization (PH-only) or only radiation pressure (RP-only) is turned on. This enables us to isolate the effect of each feedback mechanism and thus to indirectly assess their relative importance in cloud dispersal. For the fiducial cloud, we additionally run low- and high-resolution models (M1E5R20\_N128 and M1E5R20\_N512) with  $N_{\text{cell}} = 128^3$  and  $512^3$  as well as a no-feedback run (M1E5R20\_nofb), in the last of which stellar feedback is turned off. In Appendix A, we compare the results from the models with different resolution. Although star formation completes slightly later in simulations with higher resolution, the overall evolutionary behavior is qualitatively the same and key quantitative outcomes (such as the SFE) are quite close at different resolution, following a converging trend. All simulations are run over 4–7 freefall times, long enough for star formation to complete and for radiation feedback to evacuate the remaining gas from the simulation domain.

## 3. SIMULATION RESULTS

We begin by presenting the overall temporal evolution of the fiducial model M1E5R20 in Section 3.1. Other models exhibit a similar evolutionary behavior, although there are significant changes in the net SFE, timescales for star formation and cloud dispersal, and velocity of outflowing gas. These will be presented in Section 3.2–3.4.

### 3.1. Overall Evolution: Fiducial Model

Similarly to the simulations of Raskutti et al. (2016), the early evolution of our fiducial model is governed by turbulence and self-gravity. The density structure becomes increasingly filamentary as a result of shock compression. The densest regions—which may be at junctions of filaments, or simply overdense clumps within

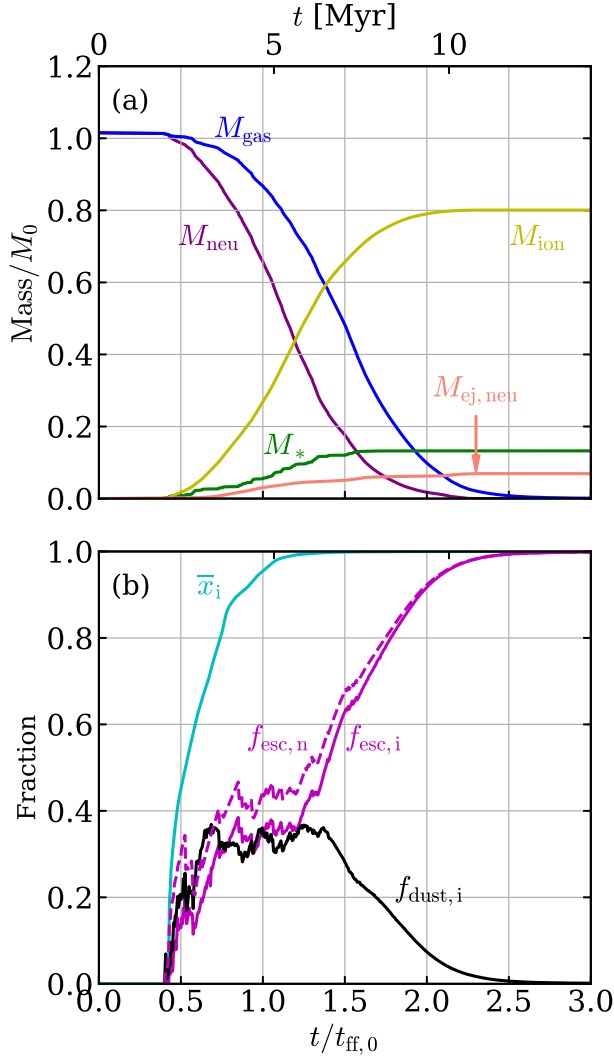


FIG. 2.— Evolutionary histories of the fiducial model with  $M_0 = 10^5 M_\odot$  and  $R_0 = 20$  pc. (a) The total gas mass  $M_{\text{gas}}$  in the simulation volume (blue), the neutral gas mass  $M_{\text{neu}}$  in the simulation volume (purple), the stellar mass  $M_*$  (green), the ejected neutral gas mass  $M_{\text{ej,neu}}$  (salmon), and the mass of the photoevaporated gas  $M_{\text{ion}}$  (yellow). (b) The volume fraction of the ionized gas  $\bar{x}_i$  (cyan), the fraction of ionizing radiation absorbed by dust  $f_{\text{dust},i}$  (black), and the escape fractions of ionizing ( $f_{\text{esc},i}$ ; solid magenta) and non-ionizing ( $f_{\text{esc},n}$ ; dashed magenta) radiation are plotted as functions of time.

filaments—undergo gravitational collapse, leading to the formation of sink particles. In the fiducial model the first collapse occurs at  $t_{*,0}/t_{\text{ff},0} = 0.4$ .

Due to star formation and the ensuing feedback, the gas in our simulations is ultimately channelled into three distinct states. One portion of the gas gravitationally collapses and is accumulated in sink particles as a total stellar mass  $M_*(t)$ . Strong ionizing radiation from newly-formed stars ionizes a portion of the initially-neutral gas, with the total mass of photoevaporated gas increasing in time as  $M_{\text{ion}}(t)$ . This includes the ionized gas currently in the simulation box and the cumulative ionized gas that has left the simulation domain. Over time, all of the neutral gas in the domain either collapses to make stars, is photoevaporated and ejected, or is ejected while

still neutral. We denote the cumulative ejected mass of the neutral gas by  $M_{\text{ej,neu}}(t)$ .<sup>4</sup> Of course, gas that is photoionized may recombine before it flows out of the box, but at the end of the simulation when no gas remains in the domain,  $M_{\text{ion,final}} = M_{\text{ion}}(t_{\text{final}})$ . The condition of mass conservation requires  $M_0 = M_{*,\text{final}} + M_{\text{ion,final}} + M_{\text{ej,neu,final}}$  at the end of the run.

Figure 2(a) plots the temporal changes of the total gas mass  $M_{\text{gas}}$  in the simulation volume as well as  $M_*$ ,  $M_{\text{ion}}$ , and  $M_{\text{ej,neu}}$ , all normalized by the initial cloud mass  $M_0$ . Figure 2(b) plots the temporal evolution of the volume filling factor of the ionized gas  $\bar{x}_i = \int (n_{\text{H}^+}/n_{\text{H}}) dV / \int dV$ , the escape fractions of ionizing ( $f_{\text{esc},i}$ ) and non-ionizing ( $f_{\text{esc},n}$ ) radiation, and the fraction of ionizing photons absorbed by dust ( $f_{\text{dust},i}$ ). These escape fractions and dust absorption fraction here are the instantaneous probabilities of escape or absorption from a single ray-trace at a given time.

Figure 3 plots selected snapshots of the fiducial model in the  $x$ - $y$  plane. From top to bottom, the rows show column density of neutral gas projected along the  $z$ -axis, slices through the stellar center of mass of the neutral hydrogen number density  $n_{\text{H}^0}$ , electron number density  $n_e$ , ionizing radiation energy density  $\mathcal{E}_i$ , non-ionizing radiation energy density  $\mathcal{E}_n$ . The projected positions of star particles are marked by circles colored by their ages. In the top row, all star particles in the simulation volume are shown, while in the bottom four rows only those within  $\Delta 5$  pc of the slice are shown. The selected times (columns from left to right) are  $t/t_{\text{ff},0} = 0.57, 0.80, 1.07$ , and  $1.40$  when 10%, 25%, 50%, and 90% of the final stellar mass has been assembled, respectively: here and hereafter, these epochs will be referred to as  $t_{*,10\%}$ ,  $t_{*,25\%}$ ,  $t_{*,50\%}$ , and  $t_{*,90\%}$ , respectively. Figure 4 displays volume rendered images of the fiducial model at these epochs.

Because of the initial turbulence, the background medium is highly clumpy and filamentary. Young H II regions formed around star particles quickly break out of their dense natal clumps, and in the larger-scale turbulent cloud some lines of sight have quite low optical depth. As a result, a substantial fraction of both ionizing and non-ionizing photons escape from the simulation box even at quite early stages of evolution. For example, at  $t_{*,10\%}$  (only  $0.17 t_{\text{ff},0} = 0.8$  Myr after the first collapse), five star particles have been created and more than 50% of computational box is filled with ionized gas, although it accounts for only 3% of the total gas mass in the domain. By this time, 13% of the radiation has escaped from the domain overall (with an instantaneous escape probability of 16%). Even though the second quadrant in the  $x$ - $y$  plane is rapidly ionized, at early times (persisting through  $t_{*,25\%}$ ) there are still regions (see lower-left panels of Figure 3) that are fully neutral because they are shadowed by dense gas that absorbs all the ionizing photons on rays emerging from the central star-forming cluster.

At  $t_{*,25\%}$ , star formation is concentrated in the central 10 pc region. Multiple H II regions expand simultaneously and merge with each other, accompanying a rapid

<sup>4</sup> We regard the neutral gas as being ejected if it reaches the outer boundary of the simulation box, although one can use a more rigorous criterion by testing the gravitational boundedness of individual gas parcels (e.g., Dale et al. 2012).



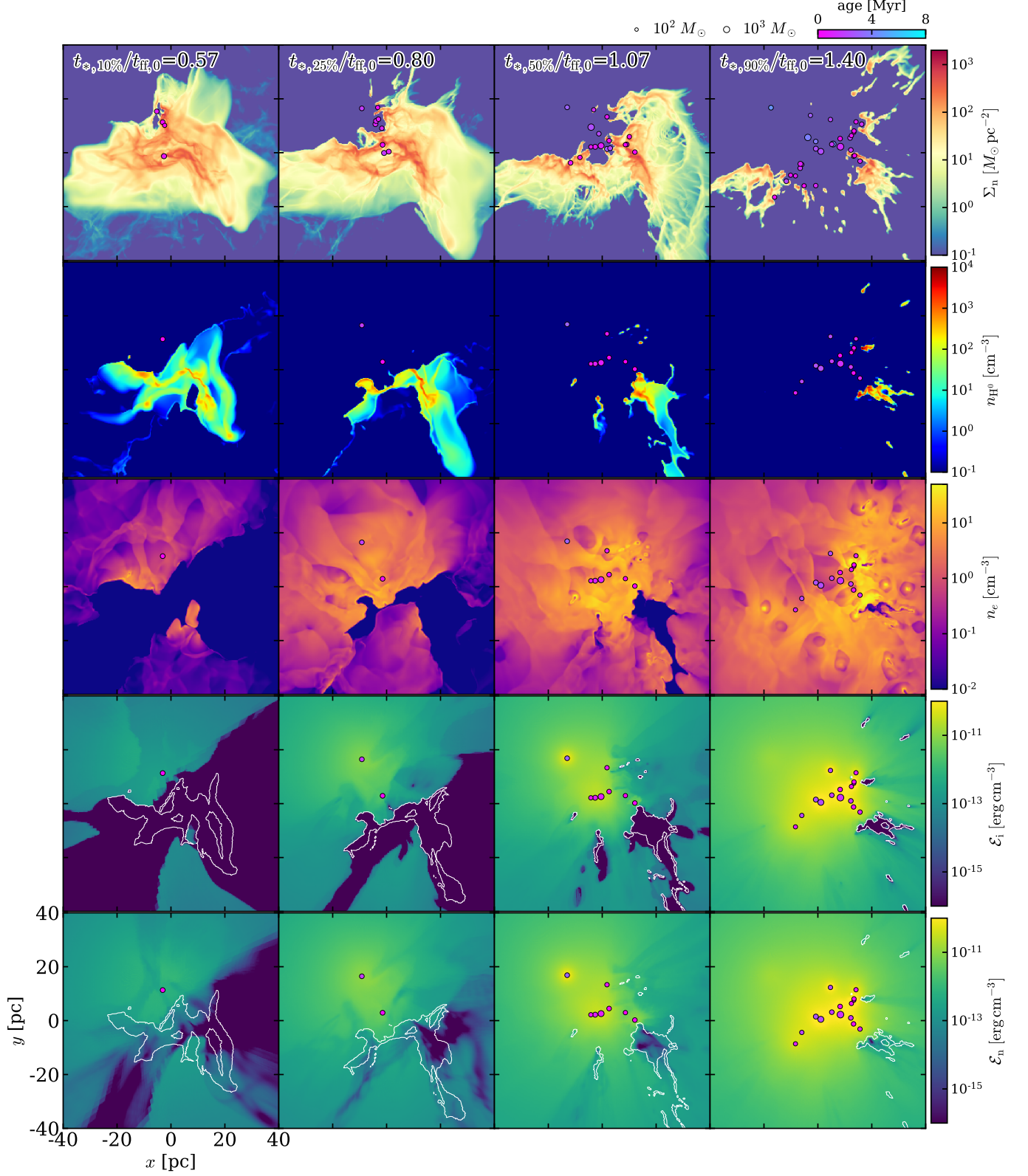


FIG. 3.— Snapshots of the fiducial model in the  $x$ - $y$  plane. The columns show times  $t/t_{\text{ff},0} = 0.58, 0.8, 1.07$ , and when 10%, 25%, 50%, 90% of the final stellar mass has been assembled, respectively. From top to bottom: surface density of neutral gas (projected along the  $z$ -axis)  $\Sigma_n$ , slices (passing through the position of the stellar center of mass) of neutral hydrogen number density  $n_{\text{H}0}$ , electron number density  $n_e$ , energy density of ionizing radiation  $\mathcal{E}_i$ , energy density of non-ionizing radiation  $\mathcal{E}_n$ . The white contours in the bottom two rows show the number density of neutral gas at  $n_{\text{H}0} = 10 \text{ cm}^{-3}$ . Small circles in each frame mark the projected positions of the star particles whose distance from the slicing plane is less than 5 pc are shown.

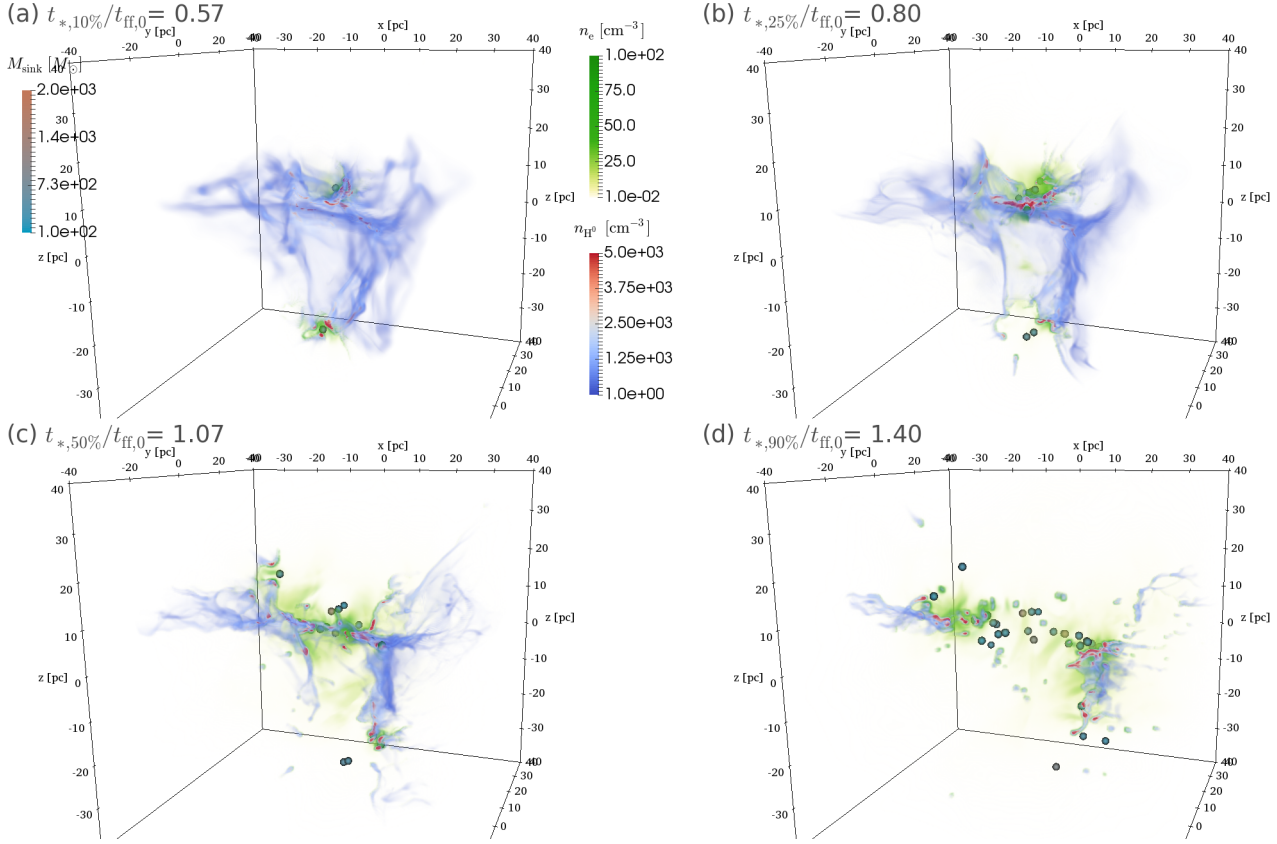


FIG. 4.— Volume rendering of the neutral hydrogen number density  $n_{\text{H}0}$  (blue-white-red) and the electron number density  $n_e$  (green-yellow) of the fiducial model at (a)  $t = t_{*,10\%}$ , (b)  $t_{*,25\%}$ , (c)  $t_{*,50\%}$ , and (d)  $t_{*,90\%}$ . Sink particles representing stellar clusters are shown as spheres colored by mass  $M_{\text{sink}}$ .

increase of  $M_{\text{ion}}$  by intense photoevaporation. Due to thermal pressure gradients, the ionized gas is pushed to the outer low-density regions, developing a roughly exponential radial density profile outside the central cavity. Ionized gas starts to escape from the box at mildly supersonic outflow velocities of  $\sim 20 \text{ km s}^{-1}$ . Simultaneously, the remaining neutral gas filaments are pushed away from the central collection of stars by a combination of radiation pressure forces and the rocket effect as gas photoevaporates from their surfaces (see top two rows of Figure 3). At later time, star formation occurs mainly in dense clumps within structures that have been pushed to the periphery of the combined H II region. We note that the expansion over time of the loci of star formation is not primarily due to shock-induced collapse as the H II region expands (collapse in filaments would have occurred anyway), but because dense gas is progressively evacuated from a larger and larger volume.

Figure 5 plots the maps of the emission measure (EM)  $\int n_e^2 dl$  integrated along the  $z$ -direction of the fiducial model at  $t_{*,10\%}$ ,  $t_{*,25\%}$ ,  $t_{*,50\%}$ , and  $t_{*,90\%}$ . In the early phase of star formation, the EM map is dominated by bright, compact H II regions around newly formed stars, while at later times it becomes rich in substructures resembling observed pillars and bright-rimmed globules (e.g., Koenig et al. 2012; Hartigan et al. 2015); these features are also apparent in the  $n_e$  slices of Figure 3. Similar structures have also been seen in previous numerical simulations of expanding H II regions in a turbulent medium (e.g., Mellema et al. 2006; Gritschneider

et al. 2009, 2010; Walch et al. 2012). The globules exhibit ionization-driven ablation flows and distinctive elongated tails pointing away from the ionizing sources. Anisotropic mass loss, preferentially from the sides of globules facing the star particles, exerts a recoil force on them; the globules rocket away from the stellar sources at a typical radial velocity of  $v_{\text{ej,neu}} \sim 5 \text{ km s}^{-1}$ .

By  $t_{*,90\%}$ , not only has the H II region engulfed the entire cloud, but the ionized region has expanded to twice the original cloud radius. Furthermore, the central 10 pc has mostly been cleared of dense gas. The escape fractions of ionizing and non-ionizing photons keep increasing with time as neutral gas surrounding ionizing sources is pushed away (see also, e.g., Rogers & Pittard 2013; Raskutti et al. 2017).

The cloud has been completely destroyed by  $t/t_{\text{ff},0} \sim 2$ , with the fraction of the remaining neutral gas  $< 2\%$  of the initial cloud mass. The final star formation efficiency is  $\varepsilon_* \equiv M_{*,\text{final}}/M_0 = 0.13$  in the fiducial model. Only 7% of the initial cloud mass is ejected in the neutral phase, while 81% is lost to photoevaporation. The remaining cluster of star particles is loosely bound gravitationally and dissolves rapidly; 30% of the final stellar mass leaves the computational domain from  $t/t_{\text{ff},0} = 2.09$  to  $t/t_{\text{ff},0} = 4$ .

### 3.2. Star Formation and Mass Loss Efficiencies

In our simulations, the SFE of a cloud rises until the associated feedback photoevaporates and dynamically ejects the remaining gas, completely halting fur-



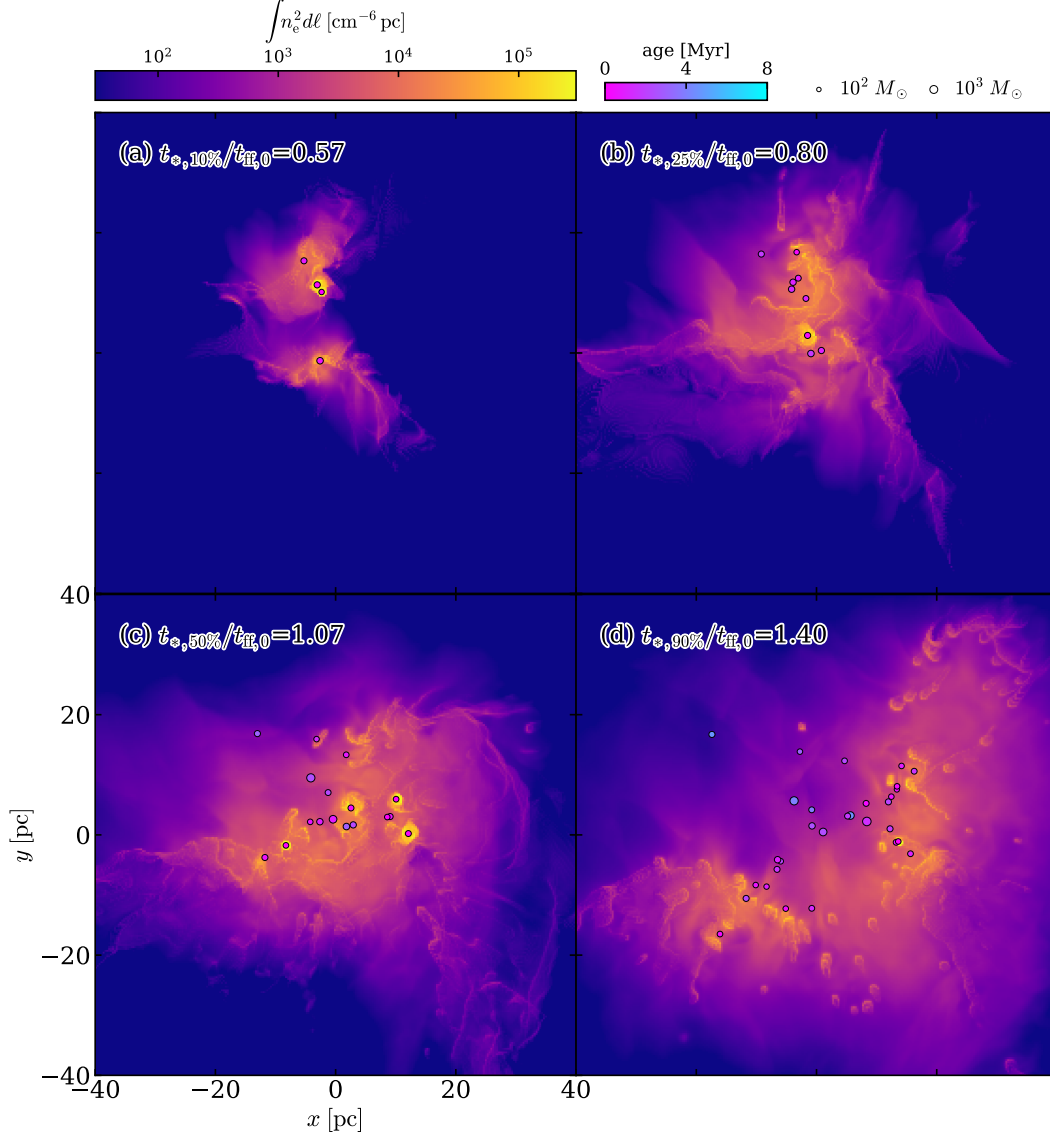


FIG. 5.— Snapshots projected on the  $x$ - $y$  plane of the emission measure of the fiducial model at (a)  $t = t_{*,10\%}$ , (b)  $t_{*,25\%}$ , (c)  $t_{*,50\%}$ , and (d)  $t_{*,90\%}$ . Circles mark the projected positions of all the star particles that have formed, with their color and size corresponding to their age and mass, respectively.

ther star formation. We define the final net SFE as  $\varepsilon_* \equiv M_{*,\text{final}}/M_0$ . In addition to the net SFE, we similarly define photoevaporation and ejection efficiencies as  $\varepsilon_{\text{ion}} \equiv M_{\text{ion},\text{final}}/M_0$  and  $\varepsilon_{\text{ej}} \equiv M_{\text{ej},\text{final}}/M_0$ , respectively, the latter of which counts both neutral and ionized gases. Note that these quantities are related by mass conservation through  $\varepsilon_{\text{ej}} = 1 - \varepsilon_* = \varepsilon_{\text{ion}} + \varepsilon_{\text{ej,neu}}$ , where  $\varepsilon_{\text{ej,neu}} \equiv M_{\text{ej,neu},\text{final}}/M_0$  and  $\varepsilon_{\text{ion}} = \varepsilon_{\text{ej,ion}}$  since no ionized gas is left inside the box at the end of the runs.

Figure 6 plots as star symbols (a) the net SFE  $\varepsilon_*$ , (b) the ejection efficiency  $\varepsilon_{\text{ej}}$ , (c) the photoevaporation efficiency  $\varepsilon_{\text{ion}}$ , and (d) the neutral ejection efficiency  $\varepsilon_{\text{ej,neu}}$  for all of our PH+RP runs as functions of the initial surface density;  $\varepsilon_*$ ,  $\varepsilon_{\text{ion}}$ , and  $\varepsilon_{\text{ej,neu}}$  are also tabulated in Columns 2–4 of Table 2. The size of the symbols represents the initial cloud mass, a convention that will be adopted throughout this paper. The net SFE depends weakly on  $M_0$  but strongly on  $\Sigma_0$ , increasing from

0.04 for M1E5R50 to 0.51 for M1E5R05. For clouds with low  $\Sigma_0$  and intermediate-to-high  $M_0$  (M5E4R15, M1E5R20, M1E5R30, M1E5R40, M1E5R50, M1E6R45, M1E6R80), photoevaporation is effective in destroying clouds:  $\varepsilon_{\text{ion}} \gtrsim 0.7$  and the resulting SFE is  $\varepsilon_* \lesssim 0.2$ . By contrast, the low mass clouds with  $M_0 = 10^4 M_\odot$  (M1E4R02, M1E4R03, M1E4R05, M1E4R08) and/or high surface density (M1E5R10, M1E5R05, M1E6R25) clouds have  $\varepsilon_{\text{ej,neu}} \gtrsim 0.1$ , implying that dynamical ejection of neutral gas is non-negligible for disruption and quenching of further star formation in these clouds.

The effect of radiation feedback on cloud disruption is limited in the highest- $\Sigma_0$  clouds such as M1E4R02, M1E5R05 and M1E6R25. These reach  $\varepsilon_* \gtrsim 0.4$  before the remaining gas is dispersed. This is due to a deep gravitational potential well, which outflowing gas must overcome to escape from the system (e.g., Dale et al. 2012). These clouds also have a comparatively dense and thick

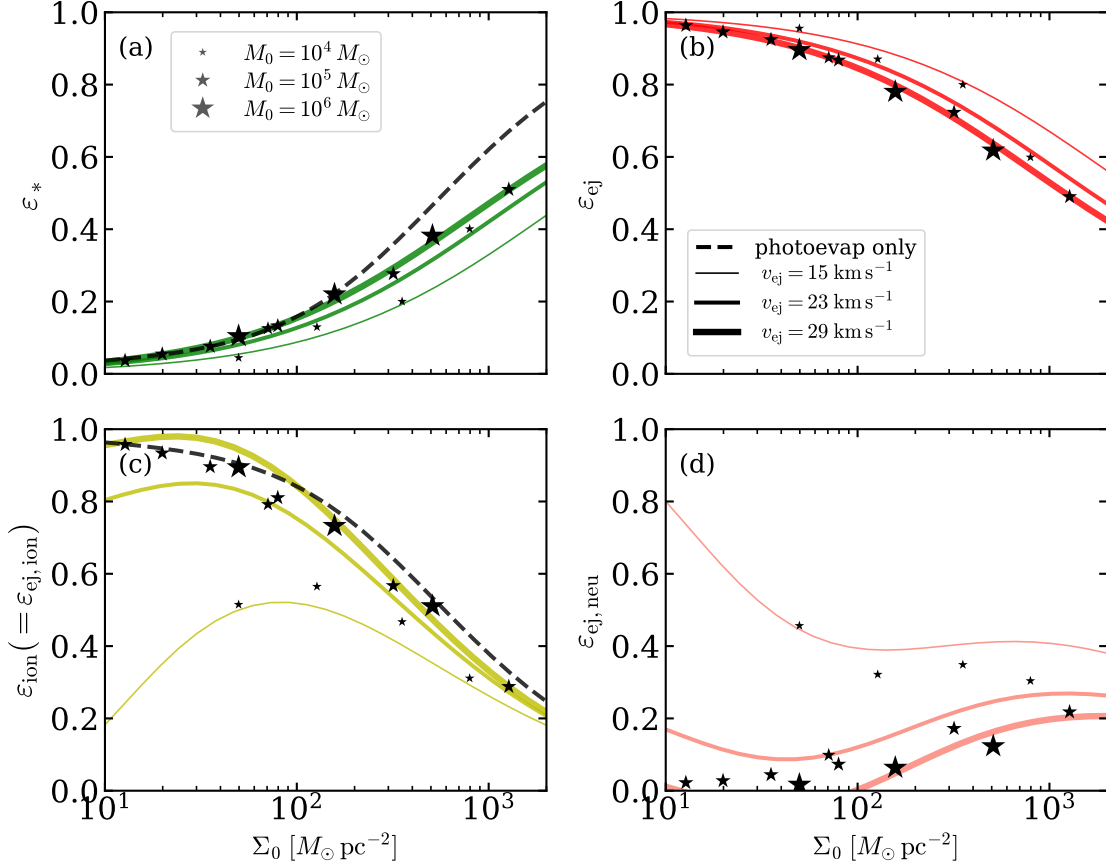


FIG. 6.— (a) Net star formation efficiency  $\varepsilon_*$ , (b) ejection efficiency  $\varepsilon_{\text{ej}}$ , (c) photoevaporation efficiency  $\varepsilon_{\text{ion}}$ , and (d) neutral ejection efficiency  $\varepsilon_{\text{ej,neu}}$  for the PH+RP runs (star symbols) as functions of the initial gas surface density  $\Sigma_0$ . The symbol size is proportional to the initial cloud mass  $M_0$  (this notation will be kept throughout this paper). Lines in each panel compare to our semi-analytic models for cloud disruption, as presented in Section 5: the dashed lines correspond to the prediction when photoevaporation dominates mass loss, while the solid lines are based on our numerical measurement of momentum injection applied to different cloud masses.

layer of recombining gas and dust that absorbs most ionizing photons, resulting in relatively inefficient photoevaporative mass loss (see Section 4.1). Thus, radiation pressure plays a relatively more important role for the highest surface density clouds.

One can assess the relative (negative) impact of photoionization and radiation pressure feedback on star formation by comparing the net SFEs of the PH-only or RP-only runs with those of PH+RP models. Figure 7 plots  $\varepsilon_*$  of PH-only (red circles), RP-only (blue squares), and PH+RP (dark stars) models as a function of  $\Sigma_0$ . Overall, the increasing trend of  $\varepsilon_*$  with  $\Sigma_0$  is similar for all models. For most of our models, the net SFE of the PH-only run is smaller than that of the RP-only counterpart and closer to that of the PH+RP run, indicating that photoionization feedback plays a more important role than radiation pressure in disrupting the parent clouds. The two exceptions are the massive, high-surface density clouds (M1E5R05 and M1E6R25), for which the net SFE of the RP-only run is smaller than that of the PH-only run.

The net SFEs of the RP-only runs lie approximately on a single sequence as a function of  $\Sigma_0$ , regardless of  $M_0$ , also in accordance with the recent theoretical predictions of the regulation of star formation by the radiation pressure feedback alone (Raskutti et al. 2016; Thompson &

Krumholz 2016). We quantitatively show in Appendix B that our RP-only results are indeed in good agreement with the analytic predictions. Our net SFE is slightly lower than those obtained in the numerical simulations of Raskutti et al. (2016), which employed a grid-based moment method for radiation. Paper I showed that this method does not adequately resolve the radiation field near individual star particles (because radiation sources have finite size), leading to more gas accretion and thus a higher SFE.

Figure 7 also shows that model M1E5R20\_nofb (green triangle) in the absence of feedback converts 87% of the gas into stars over the course of evolution. The reason that even this no-feedback run has a non-zero ejection efficiency of  $\varepsilon_{\text{ej}} = 0.13$  is that initial turbulence makes a small fraction of the gas gravitationally unbound. Raskutti et al. (2016) found that the initial “turbulent outflow ejection” efficiency is  $\varepsilon_{\text{ej,turb}} = 10\text{--}15\%$  for all models (see their Figure 17a). In principle, this can be used to derive an “adjusted” feedback-induced SFE of  $\varepsilon_{*,\text{adj}} = \varepsilon_*/(1 - \varepsilon_{\text{ej,turb}})$ .

Finally, we note that the feedback effects of photoionizing radiation and non-ionizing radiation on quenching star formation are not simply additive. If feedback effects were additive, the naive expectation would be

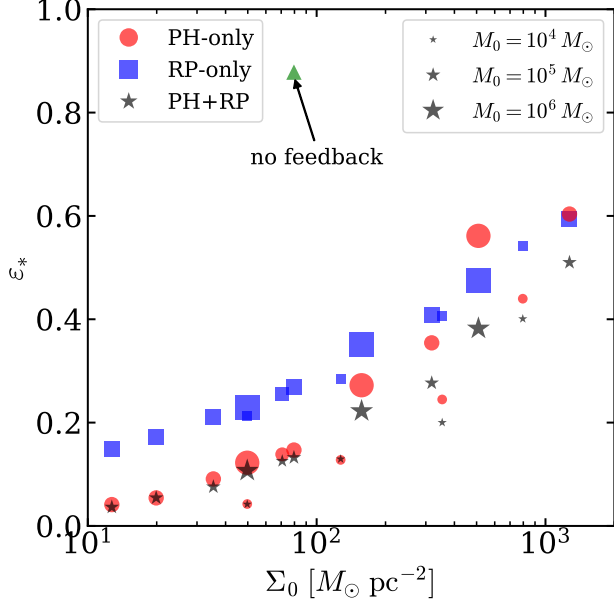


FIG. 7.— Net SFE  $\varepsilon_*$  as a function of initial surface density  $\Sigma_0$  for the models with photoionization only (PH-only, red circles), models with radiation-pressure only (RP-only, blue squares), and models with both photoionization and radiation pressure included (PH+RP, black stars). Symbol sizes denote the initial cloud mass. The green triangle represents  $\varepsilon_*$  of the fiducial cloud with no feedback. For low surface density clouds, the net SFEs of PH-only runs are smaller than that of RP-only runs and are closer to that of PH+RP runs. This suggests that photoionization is more important than radiation pressure in cloud destruction. For dense and massive clouds (M1E5R05 and M1E6R25), radiation pressure has a greater impact on cloud destruction.

$1/\varepsilon_{*,\text{PH+RP}} = 1/\varepsilon_{*,\text{PH}} + 1/\varepsilon_{*,\text{RP}}$ . However, we find that the true value of  $\varepsilon_{*,\text{PH+RP}}$  is 20–30% larger than this naive expectation.

### 3.3. Timescales for Star Formation and Cloud Destruction

The cloud lifetime is important to understanding the life cycle of GMCs within the context of other ISM phases, yet observational constraints on it remain quite uncertain (Heyer & Dame 2015). We use our simulations to directly measure the relevant timescales as follows. We define the star formation timescale in our models as the time taken to assemble 95% of the final stellar mass after the onset of radiation feedback, i.e.,  $t_{\text{SF}} \equiv t_{*,95\%} - t_{*,0}$ . The approximate gas depletion timescale by star formation is then  $t_{\text{dep}} = t_{\text{SF}}/\varepsilon_*$ . We regard a cloud as being effectively destroyed at  $t = t_{\text{neu},5\%}$  when only 5% of the initial cloud mass is left over as the neutral phase in the simulation box, with the other 95% transformed into stars, photoionized, or ejected. We define the destruction timescale as  $t_{\text{dest}} = t_{\text{neu},5\%} - t_{*,0}$ .<sup>5</sup> In most cases,  $t_{\text{dest}} > t_{\text{SF}}$ ,<sup>6</sup> but generally the two timescales are very

<sup>5</sup> For the M1E4R08 model, we take  $t_{\text{dest}}$  as the time difference between  $t_{\text{neu},5\%}$  and the time at which second sink particle formed, because the first star particle, with its small ionizing photon output rate  $Q_i \sim 2.1 \times 10^{46} \text{ s}^{-1}$ , has limited impact on the cloud evolution (see also Figure 10).

<sup>6</sup> In the M1E5R40 model, late-time star formation (roughly  $\sim 10\%$  of the final stellar mass) occurs in a dense globule even after  $t_{\text{neu},5\%}$ .

similar. Columns 5–7 of Table 2 list  $t_{*,0}$ ,  $t_{\text{SF}}$ , and  $t_{\text{dest}}$ , respectively.

Figure 8 plots  $t_{\text{SF}}$  (triangles),  $t_{\text{dest}}$  (squares), and  $t_{\text{dep}}$  (circles) of our PH+RP runs in units of Myr (left panel) and in units of the initial freefall time (right panel). In physical units,  $t_{\text{SF}}$  and  $t_{\text{dest}}$  increase from  $\sim 1\text{--}3$  Myr in the densest clouds ( $n_{\text{H},0} \gtrsim 500 \text{ cm}^{-3}$  and  $\Sigma_0 \gtrsim 300 M_\odot \text{ pc}^{-2}$ ) to  $\sim 8\text{--}14$  Myr in the lowest-density clouds ( $n_{\text{H},0} \lesssim 10 \text{ cm}^{-3}$  and  $\Sigma_0 \lesssim 20 M_\odot \text{ pc}^{-2}$ ). Relative to the freefall time,  $t_{\text{SF}}$  ( $t_{\text{dest}}$ ) decreases from  $\sim 2t_{\text{ff},0}$  ( $\sim 4t_{\text{ff},0}$ ) in the dense clouds to  $\sim 0.4t_{\text{ff},0}$  ( $\sim 0.6t_{\text{ff},0}$ ) in the low-density clouds. Our result that  $t_{\text{SF}} \lesssim 2t_{\text{ff},0}$  is consistent with the picture of rapid star formation envisaged by Elmegreen (2000). The depletion timescale decreases considerably with  $\Sigma_0$  from 250 Myr for low- $\Sigma_0$  model (M1E5R40) to 2.7 Myr for high- $\Sigma_0$  models (M1E4R02 and M1E5R05).

### 3.4. Outflow Velocity

In the presence of ionizing radiation, the outflows in our simulations consist of both neutral and ionized gas, and it is interesting to measure the dependence of ejection velocities on cloud properties. We calculate the mass-weighted ejection velocities of neutral/ionized gas as

$$v_{\text{ej,neu/ion}} = \frac{p_{\text{ej,neu/ion,final}}}{M_{\text{ej,neu/ion,final}}}, \quad (1)$$

where

$$p_{\text{ej,neu/ion,final}} = \int dt \int_{\partial V} dA \rho_{\text{neu/ion}} (\mathbf{v} \cdot \hat{\mathbf{n}}) (\mathbf{v} \cdot \hat{\mathbf{r}}) \quad (2)$$

is the time-integrated total radial momentum of neutral/ionized outflowing gas with  $\hat{\mathbf{r}}$  being the unit radial vector with respect to the stellar center of mass and  $\hat{\mathbf{n}}$  being the unit vector normal to the surface area  $dA$  at the outer boundary of the box. These values are given in Columns 9 and 10 of Table 2.

Figure 9 plots  $v_{\text{ej,neu}}$  (triangles) and  $v_{\text{ej,ion}}$  (circles) in units of  $\text{km s}^{-1}$  (left panel) and in units of the initial escape velocity  $v_{\text{esc},0}$  (right panel) for all the PH+RP runs. The outflow velocity of the ionized gas is  $\sim 18\text{--}36 \text{ km s}^{-1}$  and larger than  $v_{\text{esc},0}$  across the whole range of  $\Sigma_0$ . In low-surface density clouds, these supersonic outflows of the ionized gas are driven primarily by thermal pressure. Since ionized gas has low optical depth and hence high Eddington ratios, its ejection in high-surface density clouds is further helped by radiation pressure, while strong gravity tends to reduce the outflow velocity.

The neutral gas is ejected at a typical velocity of  $\sim 6\text{--}15 \text{ km s}^{-1}$ , about  $\sim 2\text{--}4$  times smaller than the ejection velocity of the ionized gas. This is roughly consistent with the characteristic rocket velocity  $\sim 5\text{--}10 \text{ km s}^{-1}$  of cometary globules in a photoevaporation-dominated medium (e.g., Bertoldi & McKee 1990), although the outflow velocity is also affected by gravity as well as radiation pressure forces especially for high-surface density clouds. Note that  $v_{\text{ej,neu}}/v_{\text{esc},0} \sim 0.7\text{--}2.0$  decreases slowly with increasing  $\Sigma_0$  owing to gravity.

### 4. MASS LOSS PROCESSES

For all of our simulations, radiative stellar feedback leads to at least half of the original mass in the cloud being ejected. Thus, radiation from newly formed stars



TABLE 2  
SIMULATION RESULTS

Model (1)	$\varepsilon_*$ (2)	$\varepsilon_{\text{ion}}$ (3)	$\varepsilon_{\text{ej,neu}}$ (4)	$t_{*,0}$ (5)	$t_{\text{SF}}$ (6)	$t_{\text{dest}}$ (7)	$t_{\text{ion}}$ (8)	$v_{\text{ej,neu}}$ (9)	$v_{\text{ej,ion}}$ (10)	$\langle f_{\text{ion}} \rangle$ (11)	$\langle q \rangle$ (12)
M1E5R50	0.04	0.95	0.02	0.52	0.41	0.56	0.60	8.3	24.4	0.19	61
M1E5R40	0.05	0.93	0.03	0.46	1.03	0.78	0.75	9.4	24.3	0.22	81
M1E5R30	0.08	0.89	0.04	0.44	0.72	0.95	0.98	7.8	23.9	0.24	116
M1E4R08	0.04	0.52	0.45	0.56	1.24	1.04	0.96	6.3	18.1	0.42	69
M1E6R80	0.10	0.89	0.02	0.33	0.62	0.69	0.74	10.7	26.3	0.37	320
M5E4R15	0.12	0.79	0.09	0.44	1.14	1.45	1.31	7.1	23.1	0.26	148
<b>M1E5R20</b>	<b>0.13</b>	<b>0.81</b>	<b>0.07</b>	<b>0.40</b>	<b>1.15</b>	<b>1.39</b>	<b>1.32</b>	<b>7.9</b>	<b>24.1</b>	<b>0.26</b>	<b>203</b>
M1E4R05	0.13	0.56	0.32	0.52	1.19	2.07	1.61	6.8	20.2	0.36	199
M1E6R45	0.22	0.73	0.06	0.27	1.12	1.37	1.44	13.2	28.6	0.37	753
M1E5R10	0.28	0.56	0.17	0.33	1.79	2.26	2.08	8.3	25.6	0.42	807
M1E4R03	0.20	0.47	0.34	0.44	2.13	3.16	2.48	6.0	20.9	0.36	402
M1E6R25	0.38	0.52	0.11	0.24	1.70	2.41	2.38	14.7	35.6	0.43	2032
M1E4R02	0.40	0.32	0.29	0.40	2.32	4.10	2.97	6.7	24.1	0.46	1630
M1E5R05	0.51	0.31	0.19	0.27	2.35	3.59	3.46	9.7	30.2	0.50	2950
M1E5R20_N128	0.15	0.79	0.07	0.42	0.92	1.13	1.26	8.7	23.3	0.25	261
M1E5R20_N512	0.12	0.82	0.07	0.38	1.35	1.53	1.39	7.6	24.2	0.26	188
M1E5R20_nofb	0.88	...	0.13	0.40	5.85	...	...	3.9	...	...	...

NOTE. — Column 1: model name. Column 2: net star formation efficiency. Column 3: photoevaporation efficiency. Column 4: neutral ejection efficiency. Column 5: time of first star formation (in units of  $t_{\text{ff},0}$ ). Column 6: star formation duration  $t_{\text{SF}} = t_{*,95\%} - t_{*,0}$  (units  $t_{\text{ff},0}$ ). Column 7: timescale for cloud destruction  $t_{\text{dest}} = t_{\text{neu},5\%} - t_{*,0}$  (units  $t_{\text{ff},0}$ ). Column 8: timescale for photoevaporation (units  $t_{\text{ff},0}$ ; Equation (12)). Column 9: time-averaged outflow velocity of the neutral gas ( $\text{km s}^{-1}$ ). Column 10: time-averaged outflow velocity of the ionized gas ( $\text{km s}^{-1}$ ). Column 11: time-averaged hydrogen absorption fraction (see Equation (8)). Column 12: time-averaged shielding factor. The fiducial model M1E5R20 is shown in bold.

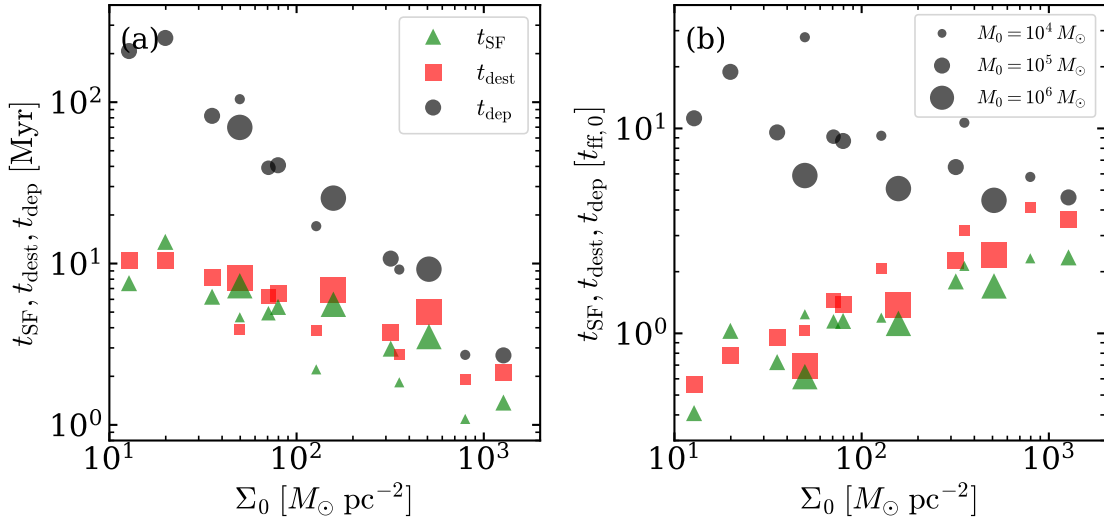


FIG. 8.— (a) Timescales for star formation  $t_{\text{SF}} = t_{*,95\%} - t_{*,0}$  (triangles), cloud destruction  $t_{\text{dest}} = t_{\text{neu},5\%} - t_{*,0}$  (squares), and effective gas depletion  $t_{\text{dep}} = t_{\text{SF}}/\varepsilon_*$  (circles) for all PH+RP models as functions of the initial cloud surface density  $\Sigma_0$ . (b) Same as (a) but with the timescales normalized by the initial freefall time  $t_{\text{ff},0}$ .

actively quenches future star formation. As Figure 6 shows, most of the ejected gas is in the ionized phase, especially for typical GMCs in normal disk galaxies with  $\Sigma_0 \lesssim 10^2 M_\odot \text{pc}^{-2}$  and  $M_0 \gtrsim 10^5 M_\odot$ . For high-density or low-mass clouds, ejection of the neutral phase is non-negligible, but  $\varepsilon_{\text{ej,neu}}$  never exceeds  $\varepsilon_{\text{ej,ion}}$ . In this section, we first develop and calibrate a simple theoretical models of mass loss by photoevaporation. We then analyze the momentum injection in our models, including both ionized and neutral gas. These results for photoevaporation and momentum injection will be used in Sec-

tion 5 to make predictions for the net SFEs and mass-loss efficiencies in comparison with our numerical results.

#### 4.1. Mass Loss by Photoevaporation

We first consider the case in which star formation is quenched solely by photoevaporation. Ionizing photons emitted by star particles arrive at ionization fronts (IFs) after passing through an intervening volume in which the gas is nearly fully ionized, with a balance between ionization and recombination. Ionized gas created at IFs does not participate in star formation (provided it remains sufficiently exposed to radiation) and will be eventually

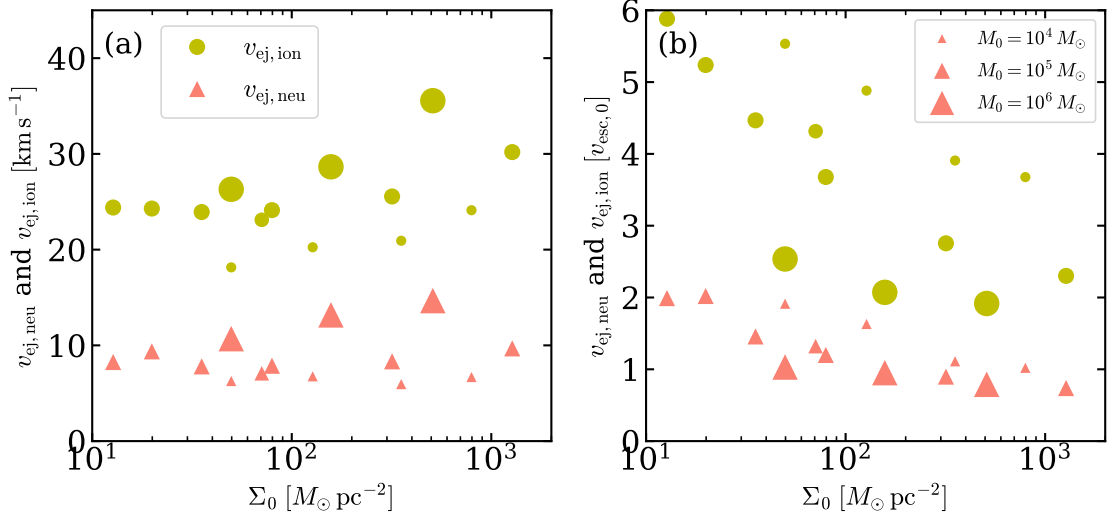


FIG. 9.— (a) Mean radial velocity of the outflowing neutral gas (triangles) and ionized gas (circles) for all PH+RP models as functions of the initial cloud surface density  $\Sigma_0$ . (b) Same as (a) but normalized by the initial escape velocity  $v_{\text{esc}, 0}$ .

pushed out of the cloud and simulation volume by thermal and radiation pressures. Here we use physical scaling arguments to estimate the net photoevaporation rate in a star-forming cloud.

#### 4.1.1. Ionization Analysis

H II regions formed in our simulations are highly irregular in shape. The EM map is dominated by pillars, ridges, and cometary globules near the H II region peripheries, as Figure 5 illustrates. Each of these bright features marks the IF on the surface of an optically-thick, neutral gas structure that is facing the ionizing sources. These neutral structures are photoevaporated as the IF advances. Since the newly ionized gas can expand into the surroundings, the IFs are typically D-critical or of strong-D type, and the ionized gas streams off the IF at approximately the sound speed and forms an ionized boundary layer (e.g., Oort & Spitzer 1955; Kahn 1969; Elmegreen 1976; Bertoldi 1989). In addition to the bright IF regions, Figures 3-5 show that there is substantial diffuse ionized gas in the volume, filling the space between and beyond the filaments and clumps of neutral gas. Along some lines of sight from stellar sources, ionizing photons moving toward optically-thin regions produce a weak-R type IF that quickly propagates out of the simulation domain, such that in those directions the H II region is effectively density bounded. In other directions, lines of sight from ionizing sources propagate through diffuse ionized gas until they end at an IF on the surface of dense neutral structure. As we will see below, almost all of the ionizations and recombinations in our simulations occur in the ionization-bounded Strömgren volume (IBSV), and ionization and recombination are in global equilibrium.

The equation for net electron production integrated over the entire domain reads

$$\dot{N}_e = \int \mathcal{I} dV - \int \mathcal{R} dV, \quad (3)$$

where  $\mathcal{I} = n_{\text{H}^0}(c\mathcal{E}_i/h\nu_i)\sigma_{\text{H}^0}$  is the photoionization rate per unit volume with  $c$  being the speed of light;  $\mathcal{R} =$

$\alpha_B n_e n_{\text{H}^+}$  is the recombination rate per unit volume, with  $\alpha_B = 3.03 \times 10^{-13} (T/8000 \text{ K})^{-0.7} \text{ cm}^3 \text{ s}^{-1}$  being the case B recombination coefficient. The rate at which ionized gas is newly created within the domain (from ionizations exceeding recombinations) is  $\dot{M}_{\text{ion}} = \mu_H \dot{N}_e$ , where  $\mu_H = 1.4m_H$  is the mean atomic mass per hydrogen. Part of this may go into an increase in the mass of ionized gas within the box, and part may go into escape of ionized gas from the domain:  $\dot{M}_{\text{ion}} = \dot{M}_{\text{ion, box}} + \dot{M}_{\text{ion, ej}}$ .

In our simulations, some fraction of the ionizing photons emitted by the stars are absorbed by neutral hydrogen, while others are absorbed by dust or escape from the simulation domain. Let  $f_{\text{ion}} = 1 - f_{\text{esc}, i} - f_{\text{dust}, i}$  denote the fraction of ionizing photons absorbed by neutral hydrogen. Then, the total photoionization rate of neutral hydrogen inside the H II region can be written as

$$\int \mathcal{I} dV = f_{\text{ion}} Q_i \equiv Q_{i, \text{eff}}. \quad (4)$$

Newly-ionized gas is created at IFs, and we denote the total effective area of these IFs as  $A_i$ . Gas streams away from the IFs with typical number density  $n_i$  and characteristic velocity  $c_i = (2.1 k_B T_{\text{ion}} / \mu_H)^{1/2} = 10.0 \text{ km s}^{-1}$  (e.g., Bertoldi 1989). We thus write

$$\dot{N}_e \equiv c_i n_i A_i \quad (5)$$

for the rate of electron production at the IFs. Equation (5) may be thought of as defining the product  $n_i A_i$  in terms of  $\dot{N}_e$ .

To reach the IFs, photons traverse a volume of nearly fully ionized gas that is undergoing recombination (which is approximately balanced by ionization; see below). If we define the effective path length through this ionized volume as  $H_i$ , we can write the total recombination rate as

$$\int \mathcal{R} dV \equiv \alpha_B n_i^2 A_i H_i. \quad (6)$$

With  $n_i A_i$  defined via Equation (5), we can think of Equation (6) as defining the ratio  $A_i / H_i$ , which has units

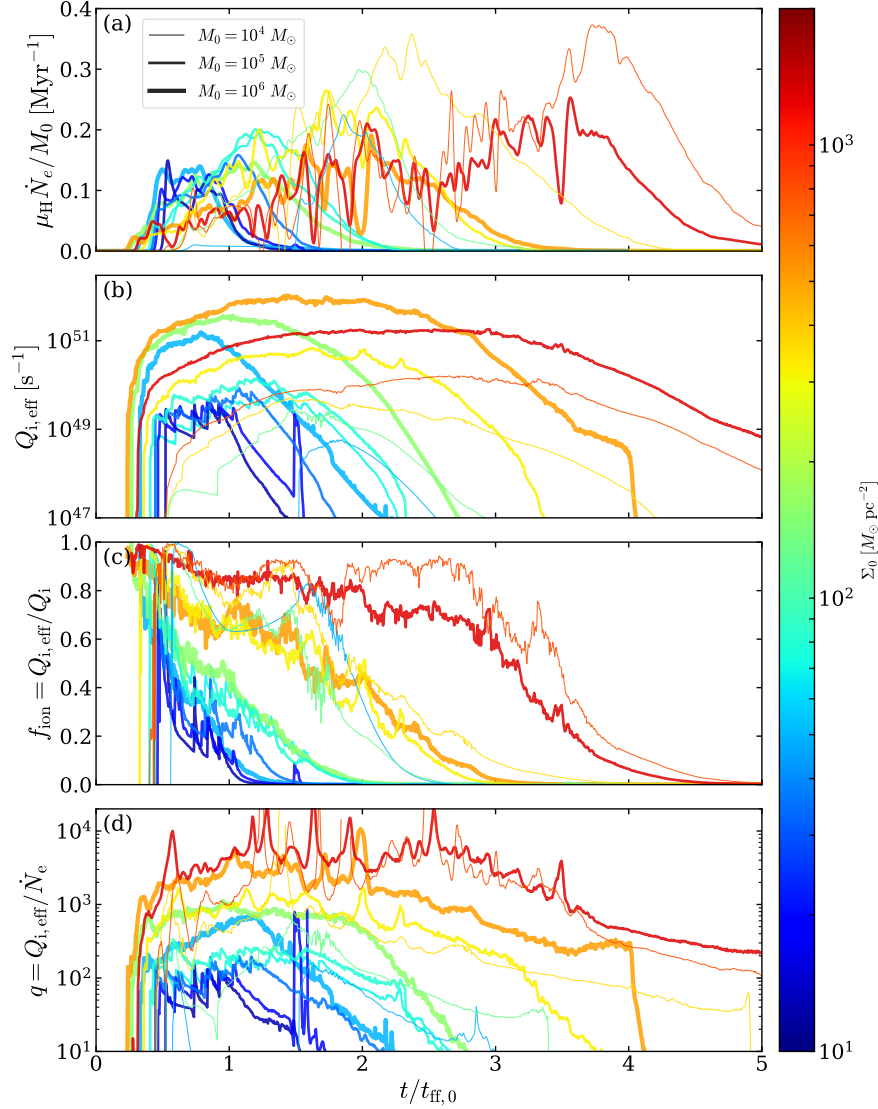


FIG. 10.— (a) Mass loss rate  $\mu_{\text{H}}\dot{N}_{\text{e}}$  via photoevaporation normalized by the initial cloud mass  $M_0$ , (b) total photoionization rate  $Q_{\text{i,eff}}$ , (c) fraction of ionizing photons absorbed by neutral hydrogen  $f_{\text{ion}} = Q_{\text{i,eff}}/Q_{\text{i}}$ , and (d) shielding factor  $q = Q_{\text{i,eff}}/\dot{N}_{\text{e}}$  as functions of time. The line color and thickness respectively correspond to the surface density and mass of the initial cloud. The shielding factor is much larger than unity in all models, indicating that most ionizing photons are used in maintaining ionization equilibrium within the H II region rather than creating new ionized gas.

of length.

The volume of highly-ionized gas between the source and the IF acts as an insulator, absorbing photons that would otherwise reach the IF in order to balance recombination. We define the ratio of available ionizing photons to photons that actually reach the IF as a shielding factor:

$$q \equiv \frac{Q_{\text{i,eff}}}{\dot{N}_{\text{e}}} = 1 + \frac{\int \mathcal{R} dV}{\int \mathcal{I} dV - \int \mathcal{R} dV} = 1 + \frac{\alpha_{\text{B}} n_{\text{i}} H_{\text{i}}}{c_{\text{i}}}. \quad (7)$$

With this definition,  $q = 1$  would imply all the ionizing photons are used to ionize neutrals at the IF, while  $q \gg 1$  when most of the ionizing photons are shielded by the IBSV. The second term on the right-hand side of Equation (7),  $\alpha_{\text{B}} n_{\text{i}} H_{\text{i}}/c_{\text{i}}$ , represents the ratio of the characteristic flow timescale to the recombination timescale, or the number of recombinations occurring over the time

it would take the flow to cross the IBSV.

Figure 10 plots the temporal histories of (a) the specific evaporation rate  $\mu_{\text{H}}\dot{N}_{\text{e}}/M_0$ , (b) the total photoionization rate  $Q_{\text{i,eff}}$ , (c) hydrogen absorption fraction of ionizing photons  $f_{\text{ion}}$ , and (d) the shielding factor  $q$ , for all of our PH+RP runs. Both the evaporation rate and photoionization rate reach peak values and then decline with time as the cloud is destroyed.

The hydrogen absorption fraction is largest in the early, embedded phase of star formation and decreases with time as optical depth drops and most of the ionizing photons escape the computational box. Column (11) of Table 2 gives

$$\langle f_{\text{ion}} \rangle \equiv \frac{\int \dot{N}_{\text{e}} f_{\text{ion}} dt}{\int \dot{N}_{\text{e}} dt}, \quad (8)$$



where the angle brackets  $\langle \rangle$  denote the  $\dot{N}_e$ -weighted temporal average over the whole simulation period after  $t_{*,0}$  (when  $\dot{N}_e$  is nonzero). The value of  $\langle f_{\text{ion}} \rangle$  ranges from 0.19 to 0.50. Overall, a larger fraction of ionizing radiation is absorbed by hydrogen in higher surface density clouds as H II regions undergo a relatively longer embedded phase.

Figure 10 shows that the shielding factor is much larger than unity for all models at all times. Column (12) of **Table 2** gives  $\dot{N}_e$ -weighted time-averaged values  $\langle q \rangle$ , which ranges from 61 to 2950, increasing with mass and surface density. This is consistent with the expectation (cf. the right-hand side of Equation (7)) that a higher recombination rate in denser clouds, as well as longer path lengths in larger clouds, increases shielding and therefore reduces the efficiency of photoevaporation.

The fact that our clouds have  $q \gg 1$  justifies the assumption of a global equilibrium between ionization and recombination

$$Q_{\text{i,eff}} = \int \mathcal{I} dV \approx \int \mathcal{R} dV = \alpha_B n_i^2 A_i H_i. \quad (9)$$

We solve this to obtain  $n_i \approx [Q_{\text{i,eff}}/(\alpha_B A_i H_i)]^{1/2}$ , and from Equation (7) we obtain the shielding factor

$$q \approx \frac{\alpha_B n_i H_i}{c_i} \approx \frac{\alpha_B^{1/2}}{c_i} \left( \frac{Q_{\text{i,eff}} H_i}{A_i} \right)^{1/2}, \quad (10)$$

while Equation (5) yields an approximate expression for the evaporation rate:

$$\dot{N}_e \approx \frac{c_i}{\alpha_B^{1/2}} \left( \frac{Q_{\text{i,eff}} A_i}{H_i} \right)^{1/2}. \quad (11)$$

The timescale for the photoevaporative mass loss tends to be longer in high surface density clouds, similarly to  $t_{\text{dest}}$  and  $t_{\text{SF}}$ . Despite the fact that they have a relatively high hydrogen absorption fraction and a small escape fraction of ionizing photons, the mass loss is inefficient because of large  $q$ . In addition, the motions of sink particles and the associated neutral envelopes cause a sudden change in the optical depth of ionizing photons. As a result, the size and shape of the H II region and photoevaporation rate fluctuate with time until they completely exhaust accretion flows and break out to larger radii at late time (e.g., [Peters et al. 2010](#); [Dale et al. 2012](#)).

We shall define the cloud photoevaporation timescale as

$$t_{\text{ion}} \equiv \frac{N_e}{\langle \dot{N}_e \rangle} = \frac{N_e^2}{\int \dot{N}_e^2 dt}, \quad (12)$$

where  $N_e = \int \dot{N}_e dt$  is the integrated number of electrons. Column (8) of **Table 2** lists the value of  $t_{\text{ion}}$  for all models. Our numerical simulations show that this timescale is typically comparable to the initial freefall timescale for the cloud,  $t_{\text{ff},0}$ .

#### 4.1.2. Constraints from Simulations

Once  $Q_{\text{i,eff}}$ ,  $A_i$ , and  $H_i$  are known, Equation (11) can be used to estimate the photoevaporation mass loss rate in star-forming clouds. It is natural to expect that the total area  $A_i$  of the ionization front scales with

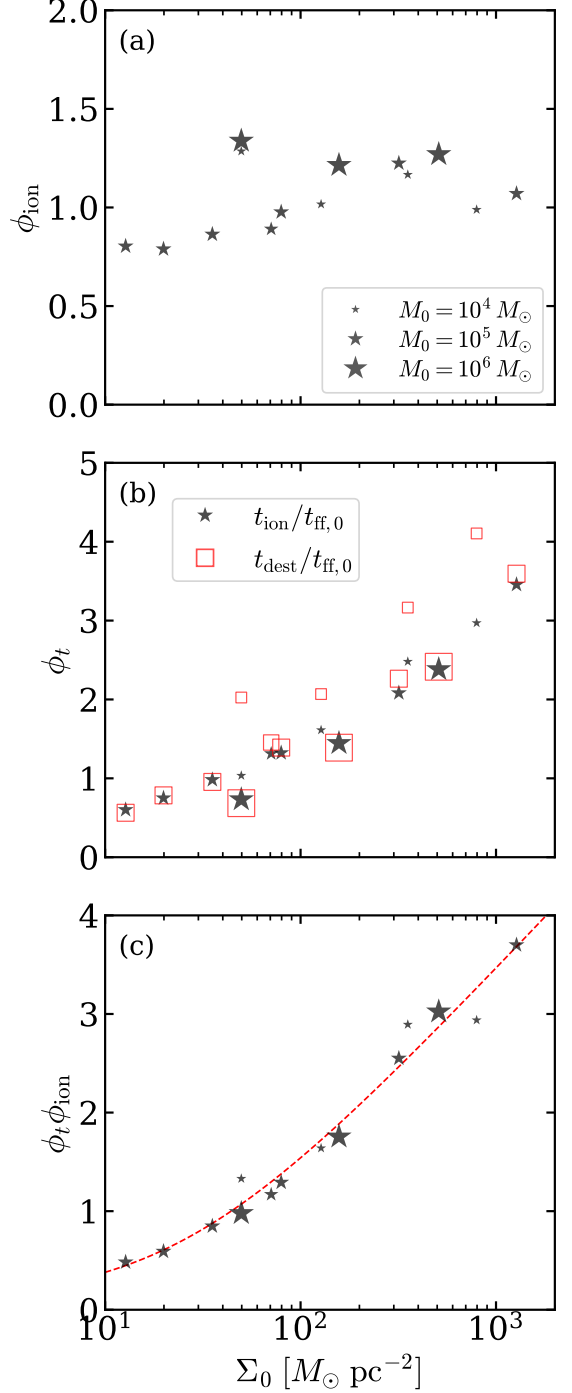


FIG. 11.— Dependence on  $\Sigma_0$  of (a) the dimensionless ionization rate  $\phi_{\text{ion}}$ , (b) the dimensionless photoevaporation timescale  $\phi_t$  for clouds, and (c) the product  $\phi_{\text{ion}} \phi_t$ , displayed as star symbols for all PH+RP models. In (b), the cloud destruction timescale  $t_{\text{dest}}/t_{\text{ff},0}$  is shown for comparison as open squares. The red dashed line in (c) is our fit to the numerical results (see Equation 16).

the surface area  $4\pi R_0^2$  of the cloud, while the thickness  $H_i$  of the IBSV scales with the cloud radius  $R_0$ . Our numerical results, based on measured  $Q_{\text{i,eff}}$ ,  $\dot{N}_e$ , and  $\int n_e^2 dV / \int n_e dV \rightarrow n_i$ , show that time-averaged values of  $A_i/(4\pi R_0^2) = \dot{N}_e/(4\pi n_i c_i R_0^2)$  and  $H_i/R_0 \approx$

$c_i Q_{i,\text{eff}}/(\alpha_B n_i \dot{N}_e R_0)$  are indeed of order unity. In detail, the time-averaged values of  $A_i/(4\pi R_0^2)$  and  $H_i/R_0$  are in the ranges 0.5–2.0 and 0.6–1.9, respectively. Motivated by Equation (11), together with the characteristic dynamical time of clouds, we introduce the dimensionless evaporation rate  $\phi_{\text{ion}}$  and evaporation timescale  $\phi_t$  defined as

$$\phi_{\text{ion}} \equiv \langle \dot{N}_e \rangle \times \frac{\alpha_B^{1/2}}{c_i Q_{i,\text{max}}^{1/2} R_0^{1/2}}, \quad (13)$$

$$\phi_t \equiv \frac{t_{\text{ion}}}{t_{\text{ff},0}}, \quad (14)$$

where  $Q_{i,\text{max}}$  is the maximum rate of the total ionizing photons over the lifetime of a star cluster (which is directly related to the SFE).

Figure 11 plots  $\phi_{\text{ion}}$  and  $\phi_t$  from our PH+RP models as star symbols. Note that  $\phi_{\text{ion}} \sim 0.79$ –1.34, roughly independent of the cloud mass and surface density. From the definition in Equation (13), an order-unity value of  $\phi_{\text{ion}}$  implies a mass-loss rate from clouds in which the characteristic velocity is the ionized-gas sound speed, the characteristic spatial scale is the size of the cloud, and the characteristic density is consistent with ionization-recombination equilibrium; comparison to Equation (11) implies that  $\langle (Q_{i,\text{eff}}/Q_{i,\text{max}})(A_i/H_i) \rangle^{1/2}/R_0^{1/2} \approx \phi_{\text{ion}} \sim 1$ .

Figure 11 shows that  $\phi_t$  ranges between 0.6 to 3.5 and increases with  $\Sigma_0$ . A typical photoevaporation timescale is thus twice the freefall time in the cloud. Plotted as open squares is the normalized destruction timescale  $t_{\text{dest}}/t_{\text{ff},0}$ . This is very close to  $\phi_t$  for low-density, massive clouds, suggesting that these clouds are destroyed primarily by photoevaporation. Low-mass and/or high-surface density clouds have a destruction timescale somewhat longer than the evaporation timescale, suggesting that cloud destruction involves ejection of neutrals (accelerated by a combination of rocket effect and radiation pressure) as well as ions.

The total number of electrons (and hence ions) created by photoevaporation over the lifetime of the cloud is  $N_e = \int \dot{N}_e dt \equiv \langle \dot{N}_e \rangle t_{\text{ion}}$ . The total mass photoevaporated from the cloud can therefore be expressed as

$$M_{\text{ion}} = \mu_H N_e = \phi_t \phi_{\text{ion}} \frac{\mu_H c_i Q_{i,\text{max}}^{1/2} R_0^{1/2} t_{\text{ff},0}}{\alpha_B^{1/2}}. \quad (15)$$

Since the right-hand side is proportional to  $M_{*,\text{final}}^{1/2}$ , this shows that the fraction of mass photoevaporated over the cloud lifetime,  $M_{\text{ion}}/M_0$ , scales as the square root (rather than linearly) of the star formation efficiency. We discuss this result further in Section 5.1. Figure 11(c) plots the product  $\phi_t \phi_{\text{ion}}$  as a function of  $\Sigma_0$ . We fit the numerical results as

$$\phi_t \phi_{\text{ion}} = c_1 + c_2 \log_{10}(S_0 + c_3), \quad (16)$$

where  $c_1 = -2.89$ ,  $c_2 = 2.11$ ,  $c_3 = 25.3$ , and  $S_0 = \Sigma_0/(M_\odot \text{pc}^{-2})$ , which is plotted as the red dashed line in Figure 11(c).

#### 4.2. Momentum Injection

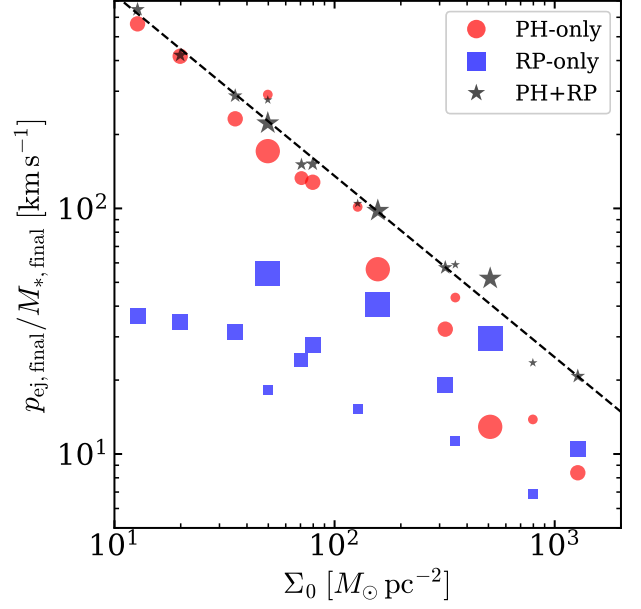


FIG. 12.— Total radial momentum yields  $p_{\text{ej,final}}/M_{*,\text{final}}$  in the PH-only (circles), RP-only (squares), and PH+RP runs (stars), as a function of the cloud surface density  $\Sigma_0$ . The dashed line shows the power-law best-fit to the numerical results of the PH+RP runs (Equation 18).

In our simulations, both neutral and ionized gas that does not collapse to make stars is eventually ejected, carrying both mass and momentum out of the cloud. In this section, we characterize the efficiency of the radial momentum injection by computing net momentum yields. We also separately assess the mean thermal and radiation pressure forces in the radial direction, where

$$\mathbf{f}_{\text{thm}} = -\nabla P, \quad \mathbf{f}_{\text{rad}} = \frac{n_{\text{H}^0} \sigma_{\text{H}^0}}{c} \mathbf{F}_i + \frac{n_{\text{H}} \sigma_{\text{d}}}{c} (\mathbf{F}_i + \mathbf{F}_n) \quad (17)$$

are the thermal and radiation pressure forces per unit volume, for  $\mathbf{F}_i$  and  $\mathbf{F}_n$  the ionizing and non-ionizing radiation fluxes, respectively.

##### 4.2.1. Net Momentum Yield

When clouds are disrupted by feedback, the resulting outflow is roughly spherical, so it is useful to measure the total radial momentum of the ejected material induced by feedback. In Section 5, we shall use the momentum ejected per unit mass of stars formed,  $p_*/m_* = p_{\text{ej,final}}/M_{*,\text{final}}$ , which here we term the net “momentum yield.”

Figure 12 plots the  $p_*/m_*$  in the PH-only (circles), RP-only (squares), and PH+RP (stars) models as a function of  $\Sigma_0$ .<sup>7</sup> We measure this by integrating the radial component of the momentum flux over the outer boundary of the simulation and over all time,  $\int dt \int_{\partial V} dA \rho \mathbf{v} \cdot \hat{\mathbf{n}} \cdot \hat{\mathbf{r}}$ , where  $\hat{\mathbf{n}}$  is the normal to area  $dA$ . The PH-only runs have momentum yields higher than the RP-only results except for models M1E5R05 and M1E6R25, and close to

<sup>7</sup> A small fraction of the outflow momentum is associated with the initial radial component of the turbulent outflow. For the fiducial cloud with no radiation feedback, the final outflow momentum is 3% of that of the PH+RP run.

the PH+RP results. Similarly to Figure 7, this implies that thermal pressure induced by photoionization controls the dynamics of H II regions in low surface density clouds, while radiation pressure is more important in dense, massive clouds. For the PH+RP and PH-only models, most of the outflow momentum is deposited in the ionized rather than neutral gas. We find that the total momentum yields in the PH+RP runs are well described by a power-law relationship

$$p_*/m_* = \frac{p_{\text{ej,final}}}{M_{*,\text{final}}} = 135 \text{ km s}^{-1} \left( \frac{\Sigma_0}{10^2 M_\odot \text{ pc}^{-2}} \right)^{-0.74}, \quad (18)$$

shown as the dashed line in Figure 12.

We note that by adopting a light-to-mass ratio that is time-independent, our numerical results are likely to overestimate the true feedback strength, especially for clouds with the destruction timescale longer than  $t_{\text{SN}} = 3 \text{ Myr}$  or  $t_{\text{UV}} = 8 \text{ Myr}$ . Even with this overestimation, our results show that the momentum injection to the large-scale ISM from both ionizing and non-ionizing radiation feedback is substantially smaller than that from supernovae feedback,  $p_*/m_* \sim 10^3 \text{ km s}^{-1}$  (e.g., Kim & Ostriker 2015; Kim et al. 2017). Thus, while momentum injection from radiation feedback is quite important on the spatial scale of individual clouds and early life of clusters, it is subdominant in the large-scale ISM compared to other forms of massive-star momentum injection, and is therefore not expected to be important in regulating either large-scale ISM pressure and star formation rates (e.g. Ostriker & Shetty 2011; Kim et al. 2013) or galaxy formation (e.g. Naab & Ostriker 2017).

#### 4.2.2. Efficiency of Radial Momentum Injection

Dynamical expansion of a spherical, embedded H II region in a uniform medium is well described by the thin-shell approximation. Force balance  $\mathbf{f}_{\text{thm}} + \mathbf{f}_{\text{rad}} = 0$  holds in the interior (Draine 2011) and most of the swept-up gas is compressed into a thin shell that expands due to the contact forces on it. The effective momentum injection rate from gas pressure and direct radiation pressure are  $\rho_i c_i^2 A_i$  and  $L/c$ , respectively (Krumholz & Matzner 2009; Kim et al. 2016). The former expression multiplied by a factor two has also been applied for blister H II regions, assuming that in addition to thermal pressure the cloud back-reacts to photoevaporation from a D-critical IF with  $\rho_i c_i^2 A_i = \dot{M}_{\text{ion}} c_i$  (e.g., Matzner 2002; Krumholz et al. 2006). In analytic solutions, the ionized-gas density  $\rho_i$  estimate assumes uniform density and ionization equilibrium. For either embedded or blister H II regions, this leads to an expression for momentum injection that is given by Equation (11) for  $\dot{N}_e$  multiplied by  $\mu_{\text{H}} c_i$  times an order-unity factor. For an idealized, dust-free, spherical, embedded H II region, the theoretical point of comparison for the gas pressure force is  $\mu_{\text{H}} c_i^2 (12\pi Q_i R_0 / \alpha_{\text{B}})^{1/2}$ .

In reality, H II regions possess many holes and ionizing sources are widely distributed in space. The momentum injection is then expected to be less efficient than in the idealized spherical case for the following reasons. First, the non-spherical distribution of radiation sources leads to momentum injection cancellation. Second, for applying back-reaction forces, normal vectors to irregular-

shaped cloud surfaces have non-radial components with respect to the cluster center. Third, radiation escapes through holes (see also Dale 2017; Raskutti et al. 2017). Nevertheless, the results in Section 4.1.2 show that the numerically-computed mass-loss rates from photoevaporation are similar to the predictions from dimensional-analysis scaling arguments, so we may analogously expect the radial momentum injection rate from thermal pressure to be comparable to  $\dot{M}_{\text{ion}} c_i$ . This will be lower than the idealized spherical momentum injection because dust absorption and escape of radiation reduce  $Q_{\text{i,eff}}$  below  $Q_i$ . Similarly, the radiation pressure applied to the cloud would be reduced to  $(1 - f_{\text{esc}})L/c$  by the escape of radiation, where  $f_{\text{esc}} = (L_{\text{i,esc}} + L_{\text{n,esc}})/L$  is the overall escape fraction of UV radiation; the total radiation force may be further reduced by lack of spherical symmetry.

To determine the degree of reduction in the radial momentum injection, we calculate the time-averaged, normalized thermal pressure force

$$\phi_{\text{thm}} \equiv \frac{\int_{t_i}^{t_f} \int \mathbf{f}_{\text{thm}} \cdot \hat{\mathbf{r}} dV dt}{\int_{t_i}^{t_f} \mu_{\text{H}} c_i^2 (12\pi Q_i R_0 / \alpha_{\text{B}})^{1/2} dt}, \quad (19)$$

$$\phi'_{\text{thm}} \equiv \frac{\int_{t_i}^{t_f} \int \mathbf{f}_{\text{thm}} \cdot \hat{\mathbf{r}} dV dt}{\int_{t_i}^{t_f} \dot{M}_{\text{ion}} c_i dt} \quad (20)$$

and normalized radiation pressure force

$$\phi_{\text{rad}} \equiv \frac{\int_{t_i}^{t_f} \int \mathbf{f}_{\text{rad}} \cdot \hat{\mathbf{r}} dV dt}{\int_{t_i}^{t_f} L/c dt}, \quad (21)$$

$$\phi'_{\text{rad}} \equiv \frac{\int_{t_i}^{t_f} \int \mathbf{f}_{\text{rad}} \cdot \hat{\mathbf{r}} dV dt}{\int_{t_i}^{t_f} (1 - f_{\text{esc}})L/c dt}, \quad (22)$$

where the range of time integration is taken as  $(t_i, t_f) = (t_{*,0}, t_{\text{ej},95\%})$ .<sup>8</sup>

In the above, we consider both the radial momentum injection from thermal pressure and radiation pressure relative to the maximum for a spherical shell, and relative to the actual material and radiation momentum available.

Figure 13 plots the normalized forces  $\phi_{\text{thm}}$  (circles),  $\phi'_{\text{thm}}$  (diamonds),  $\phi_{\text{rad}}$  (squares), and  $\phi'_{\text{rad}}$  (triangles) averaged over the time interval  $(t_{*,0}, t_{\text{ej},95\%})$  as functions of  $\Sigma_0$ . There is significant reduction in both the gas and radiation pressure forces compared to the prediction for the “spherical maximum”; the normalized gas pressure force  $\phi_{\text{thm}}$  is in the range 0.10–0.19 with a mean value 0.13, roughly independent of  $\Sigma_0$ ;  $\phi_{\text{rad}}$  is as small as 0.06 for model M1E5R50 and increases to 0.27 for high surface-density clouds. The values of  $\phi'_{\text{thm}}$  range from 0.67 to 1.26, suggesting that the time-averaged radial momentum injection from thermal pressure force is within  $\sim 30\%$  of the naive estimate  $\dot{M}_{\text{ion}} c_i$ . The values of  $\phi'_{\text{rad}}$  are slightly larger than  $\phi_{\text{rad}}$  and in the range 0.3–0.5, indicating that the momentum injection by radiation pres-

<sup>8</sup> The cumulative momentum injection efficiencies  $\phi_{\text{thm/rad}}$  become smaller for larger  $t_f$  since most photons escape at late time. For example,  $t_f = t_{*,0} + t_{\text{dest}}$  increases  $\phi_{\text{thm/rad}}$  by  $\sim 30\text{--}50\%$  compared to the case with  $t_f = t_{\text{ej},95\%} (> t_{\text{dest}})$ .



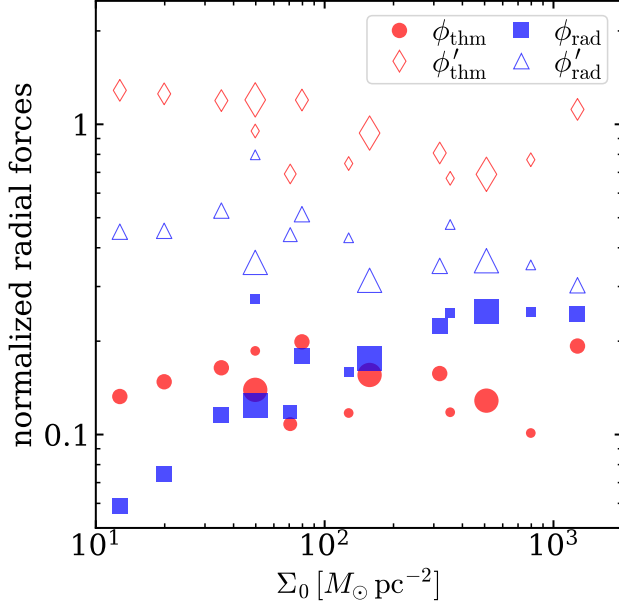


FIG. 13.— Average rates of the radial momentum injection due to gas pressure normalized by  $\mu_{\text{H}} c_i^2 (12\pi Q_i R_0 / \alpha_{\text{B}})^{1/2}$  (circles) and by  $\dot{M}_{\text{ion}} c_i$  (diamonds), due to radiation pressure normalized by  $L/c$  (squares) and  $(1 - f_{\text{esc}})L/c$  (triangles) for all the PH+RP models (see Equations (19)–(22)).

sure force is reduced by a factor of  $\sim 2$ –3 by flux cancellation alone.<sup>9</sup>

Finally, we evaluate the relative importance of gas and radiation pressure forces in radial momentum injection for the PH+RP models. Figure 14 plots the total injected momentum from gas (circles) and radiation (squares) pressure forces per unit mass of stars formed:

$$\frac{p_{\text{ej,thm}}}{M_{*,\text{final}}} \equiv \frac{\iint \mathbf{f}_{\text{thm}} \cdot \hat{\mathbf{r}} dV dt}{M_{*,\text{final}}}, \quad (23)$$

$$\frac{p_{\text{ej,rad}}}{M_{*,\text{final}}} \equiv \frac{\iint \mathbf{f}_{\text{rad}} \cdot \hat{\mathbf{r}} dV dt}{M_{*,\text{final}}}. \quad (24)$$

The results show trends similar to those exhibited by the total radial momentum yield in Figure 12 for models PH vs. RP; while the momentum injection due to gas pressure dominates in low surface density clouds, radiation pressure takes over for clouds with  $\Sigma_0 \gtrsim 500 M_{\odot} \text{pc}^{-2}$ . Our numerical results are consistent with the qualitative trend in the previous analytic models (Krumholz & Matzner 2009; Fall et al. 2010; Murray et al. 2010; Kim et al. 2016) in which radiation pressure becomes relatively more important compared to ionized-gas pressure for more massive, high surface density clouds.

Comparison of the dashed line (Equation (18)) and symbols in Figure 14 shows that the sum of injected momentum from gas and radiation pressure forces  $p_{\text{ej,thm}} + p_{\text{ej,rad}}$  is not necessarily equal to the total momentum of outflowing gas  $p_{\text{ej,final}}$ . This difference arises because of the additional centrifugal and gravitational acceleration that contributes significantly to the latter.

<sup>9</sup> Relatively high values of  $\phi_{\text{rad}}$  and  $\phi'_{\text{rad}}$  for M1E4R08 model are likely caused by the fact that feedback is dominated by a single cluster particle that accounts for 75% of the final stellar mass.

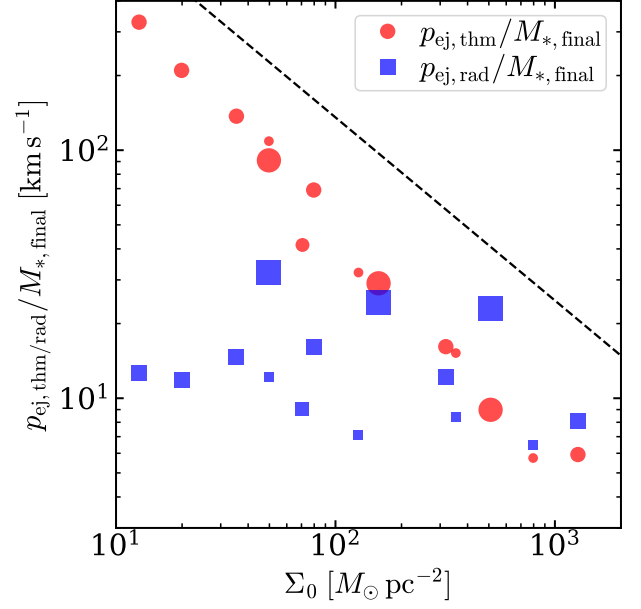


FIG. 14.— Injected radial momentum due to gas pressure (circles) and radiation pressure (squares) forces normalized by the final stellar mass  $M_{*,\text{final}}$  for all the PH+RP models (see Equations (23) and (24)). The fit to the total momentum yield, Equation (18), is shown for comparison as a dashed line.

## 5. MODELS FOR CLOUD DISPERSAL AND SFE

In this section, we use the photoevaporation rate and the momentum yield presented in the preceding section to develop semi-analytic models for cloud dispersal. We consider two models. First, we use the expected physical scaling relationship between photoevaporation and star formation efficiency (see Equation 15) to obtain a prediction for the SFE in the case that cloud destruction is mostly via ionization. In the second model, we use our numerical results for momentum injection per unit mass of stars formed to determine the SFE necessary to eject the remaining material (both ions and neutrals) from the cloud.

### 5.1. Destruction by Photoevaporation

We first consider a situation where the gas left over from star formation is all evaporated by photoionization. In this case, mass conservation requires

$$1 = \varepsilon_* + \varepsilon_{\text{ion}}, \quad (25)$$

where  $\varepsilon_{\text{ion}} = M_{\text{ion}}/M_0 = \mu_{\text{H}} N_e/M_0$ .

Using Equation (15), we express  $\varepsilon_{\text{ion}}$  as

$$\varepsilon_{\text{ion}} = \phi_t \phi_{\text{ion}} \left( \frac{\Sigma_{\text{ion}}}{\Sigma_0} \right) \varepsilon_*^{1/2}, \quad (26)$$

where

$$\Sigma_{\text{ion}} = \mu_{\text{H}} c_i \left( \frac{\Xi}{8G\alpha_{\text{B}}} \right)^{1/2} \quad (27)$$

$$= 140 \left( \frac{\Xi}{5.05 \times 10^{46} \text{ s}^{-1} M_{\odot}^{-1}} \right)^{1/2} \left( \frac{T_{\text{ion}}}{8000 \text{ K}} \right)^{0.85} M_{\odot} \text{pc}^{-2}, \quad (28)$$

with  $\Xi = Q_{i,\max}/M_{*,\text{final}}$  being the conversion factor between stellar mass and ionizing photon output. Since  $\phi_{\text{ion}}$  is roughly constant in our numerical results, Equation (26) implies that the evaporation efficiency depends linearly on the duration (relative to  $t_{\text{ff}}$ ) of photoevaporation,  $\phi_t$  (Equation (14)), and the square root of the SFE, and inversely on the cloud surface density  $\Sigma_0$ . The characteristic surface density  $\Sigma_{\text{ion}}$  can be regarded as a constant for most of the models since  $M_{*,\text{final}} > 10^3 M_\odot$ , while it varies sensitively with  $M_{*,\text{final}}$  in models with  $M_{*,\text{final}} < 10^3 M_\odot$ , as described in Section 2.1. The dependence of  $\varepsilon_{\text{ion}}$  on  $\varepsilon_*^{1/2}$  (rather than  $\varepsilon_*$ ) is caused by shielding within the IBSV, which makes photoevaporation inefficient. Most photons are used up in offsetting recombination within the H II region, rather than in eroding neutral gas to create new ions at IFs.

We solve Equations (25) and (26) for  $\varepsilon_*$  to obtain

$$\varepsilon_* = \left( \frac{2\xi}{1 + \sqrt{1 + 4\xi^2}} \right)^2, \quad (29)$$

where  $\xi \equiv \Sigma_0/(\phi_t \phi_{\text{ion}} \Sigma_{\text{ion}})$ . In the limit  $\xi \ll 1$ ,  $\varepsilon_* \approx \xi^2 = [\Sigma_0/(\phi_t \phi_{\text{ion}} \Sigma_{\text{ion}})]^2$ , while in the limit  $\xi \gg 1$ ,  $\varepsilon_* \approx 1 - 1/\xi = 1 - \phi_t \phi_{\text{ion}} \Sigma_{\text{ion}}/\Sigma_0$ . The limiting behavior shows that photoevaporation becomes very efficient for destroying clouds when  $\Sigma_0 \lesssim \Sigma_{\text{ion}}$ .

Inserting the fit for  $\phi_t \phi_{\text{ion}}$  of Equation (16) in Equation (29) allows us to calculate the net SFE as a function of  $\Sigma_0$ . The resulting  $\varepsilon_*$  and  $\varepsilon_{\text{ion}}$  are compared to the numerical results as dashed lines in Figure 6(a) and (c). For low-surface density and massive clouds with  $\varepsilon_{\text{ion}} \gtrsim 0.7$ , the semi-analytic  $\varepsilon_*$  agrees with the numerical results extremely well. The agreement is less good, however, for high-surface density ( $\Sigma_0 \gtrsim 300 M_\odot \text{ pc}^{-2}$ ) or low-mass ( $M_0 = 10^4 M_\odot$ ) clouds for which neutral gas ejection cannot be ignored; we address this next.

### 5.2. Destruction by Dynamical Mass Ejection

We consider the general case in which radiative feedback from star formation exerts combined thermal and radiation pressure forces on the surrounding gas. The gas is ejected from the cloud, quenching further star formation. In our simulations, the momentum ejected from the computational domain also includes a small contribution from the initial turbulence, which ejects a mass fraction  $\varepsilon_{\text{ej,turb}} = M_{\text{ej,turb}}/M_0 \sim 0.1$  when the cloud is initially marginally bound.

Let  $v_{\text{ej}}$  denote the characteristic ejection velocity of the outgoing gas, and let  $p_*/m_*$  denote the momentum per stellar mass injected by feedback. The total momentum of the ejected gas can be written as

$$p_{\text{ej,tot}} = (1 - \varepsilon_*)M_0 v_{\text{ej}} = (p_*/m_*)\varepsilon_* M_0 + \varepsilon_{\text{ej,turb}} M_0 v_{\text{ej}}. \quad (30)$$

We divide the both sides of Equation (30) by  $M_0 v_{\text{ej}}$  to obtain

$$\varepsilon_* = \frac{1 - \varepsilon_{\text{ej,turb}}}{1 + (p_*/m_*)/v_{\text{ej}}}. \quad (31)$$

From the results of model `M1E5R20_nofb` (see Table 2), we take  $\varepsilon_{\text{ej,turb}} = 0.13$ .<sup>10</sup> For  $v_{\text{ej}}$ , we

take the mass-weighted outflow velocity  $(\varepsilon_{\text{ej,neu}} v_{\text{ej,neu}} + \varepsilon_{\text{ej,ion}} v_{\text{ej,ion}})/\varepsilon_{\text{ej}}$ , which is found to be roughly constant for fixed  $M_0$  with mean values 15, 23, 29 km s<sup>-1</sup> for  $M_0 = 10^4, 10^5, 10^6 M_\odot$ , respectively. Equation (31) gives  $\varepsilon_*$  as functions of  $M_0$  and  $\Sigma_0$  once  $p_*/m_*$ ,  $v_{\text{ej}}$  and  $\varepsilon_{\text{ej,turb}}$  are specified. A fit to the momentum yield  $p_*/m_*$  from our numerical results as a function of  $\Sigma_0$  is given in Equation (18). Altogether, Equation (31) then gives  $\varepsilon_*$  as a function of  $M_0$  and  $\Sigma_0$ . For  $p_*/m_* \gg v_{\text{ej}}$  and  $\varepsilon_{\text{ej,turb}} \ll 1$ , the predicted scaling dependence is  $\varepsilon_* \sim v_{\text{ej}}/(p_*/m_*) \propto v_{\text{ej}} \Sigma_0^{3/4}$ .

Figure 6 overplots as solid lines the resulting (a) net SFE  $\varepsilon_*$ , (b) ejection efficiency  $\varepsilon_{\text{ej}} = 1 - \varepsilon_*$ , (c) photoevaporation efficiency  $\varepsilon_{\text{ion}}$  calculated from Equation (26), and (d) neutral ejection efficiency  $\varepsilon_{\text{ej,neu}} = \varepsilon_{\text{ej}} - \varepsilon_{\text{ion}}$ . The line thickness indicates the initial cloud mass. Overall, our semi-analytic model for the dynamical mass ejection reproduces the net SFE of the simulations fairly well, with the average difference of 0.03. The model also explains the increasing tendency of  $\varepsilon_*$  with increasing  $M_0$ . This weak dependence of the semi-analytic  $\varepsilon_*$  on  $M_0$  comes directly from  $v_{\text{ej}}$ , indicating that stronger feedback is required to unbind gas in a more massive cloud (e.g., Kim et al. 2016; Rahner et al. 2017). A drop in the photoevaporation efficiency with decreasing  $\Sigma_0$  for  $M_0 = 10^4 M_\odot$  and  $\Sigma_0 \lesssim 10^2 M_\odot \text{ pc}^{-2}$  is caused by the steep dependence of  $\Xi$  on  $M_{*,\text{final}}$  below  $10^3 M_\odot$ , as mentioned above.

## 6. SUMMARY AND DISCUSSION

In this work, we have used our new implementation of adaptive ray tracing in the *Athena* magnetohydrodynamics code to simulate star cluster formation and the effects of radiation feedback on turbulent GMCs. We consider a suite of clouds (initially marginally bound) with mass  $M_0 = 10^4$ – $10^6 M_\odot$  and radius  $R_0 = 2$ – $80 \text{ pc}$ ; the corresponding range of the surface density is  $\Sigma_0 \approx 13$ – $1300 M_\odot \text{ pc}^{-2}$ . The primary goals of the current paper are to understand the role of (ionizing and non-ionizing) UV radiation feedback in controlling the net SFE and GMC lifetime and to assess the relative importance of photoionization and radiation pressure in various environments. We augment and compare our numerical results with semi-analytic models.

Our main findings are summarized as follows.

### 6.1. Summary

#### 1. Evolutionary stages

All clouds in our simulations go through the following evolutionary stages (Figure 3), with some overlap and varying duration. (1) The initial turbulence creates filaments, and within these denser clumps condense. Some clumps undergo gravitational collapse and form star particles representing subclusters. (2) Individual H II regions form around each subcluster, growing towards directions of low optical depth until they merge and break out of the cloud. Simultaneously, both low- and high-density gas is accelerated away from the radiation sources due to thermal and radiation pressures. (3)

ran a suite of ‘no-feedback’ simulations and found that clouds with  $\alpha_{\text{vir},0} = 2$  have roughly the same turbulence ejection efficiencies  $0.10 < \varepsilon_{\text{ej,turb}} < 0.15$  regardless of  $M_0$  and  $\Sigma_0$ .

<sup>10</sup> Similar to our `M1E5R20_nofb` model, Raskutti et al. (2016)

At late stages of evolution the brightest EM features are small globules, pillars, and ridges marking individual IFs at the periphery of the H II region, quite similar to observed clouds (Figure 5). (4) At the end of the simulation, all of the gas has either collapsed into stars or been dispersed, flowing out of the computational domain.

## 2. Timescales

Cloud destruction takes  $\sim 2\text{--}10$  Myr after the onset of massive star formation feedback (Figure 8(a)). In units of the freefall time, the destruction timescale is in the range  $0.6 < t_{\text{dest}}/t_{\text{ff},0} < 4.1$  and systematically increases with  $\Sigma_0$  (Figure 8(b)). The timescale for star formation is comparable to or somewhat smaller than the destruction timescale. The effective gas depletion timescale ranges from 250 Myr to 2.7 Myr, sharply decreasing with increasing  $\Sigma_0$ .

## 3. Star formation and mass loss efficiencies

We examine the dependence on the cloud mass and surface density of the net SFE  $\varepsilon_*$ , photoevaporation efficiency  $\varepsilon_{\text{ion}}$ , and mass ejection efficiency  $\varepsilon_{\text{ej}}$  (Figure 6). The SFE ranges over  $\varepsilon_* = 0.04\text{--}0.51$ , increasing strongly with the initial surface density  $\Sigma_0$  while increasing weakly with the initial cloud mass  $M_0$ . Photoevaporation accounts for more than 70% of mass loss for clouds with  $M_0 \gtrsim 10^5 M_\odot$  and  $\Sigma_0 \lesssim 10^2 M_\odot \text{pc}^{-2}$ . The ejection of neutral gas mass by thermal and radiation pressures also contributes in quenching further star formation in low-mass and high-surface density clouds. The comparison of the net SFE among the models in which we turn on and off photoionization and radiation pressure suggests that photoionization is of greater importance in destroying GMCs in normal disk galaxies, whereas radiation pressure is more effective in regulating star formation in dense, massive clouds (Figure 7; see also Figure 14). This controlled experiment also demonstrates that the combined effects of photoionization and radiation pressure do not work in a simply additive manner in suppressing star formation.

## 4. Photoevaporation

The photoevaporation rate  $\dot{N}_e$  (the number of free electrons produced per unit time) at IFs within the cloud is much smaller than the total number of ionizing photons absorbed by hydrogen per unit time  $Q_{\text{i,eff}}$  throughout the cloud (Figure 10). Most of the ionizations instead offset recombinations in diffuse gas throughout the cloud. The time-averaged hydrogen absorption fraction  $\langle f_{\text{ion}} \rangle = \langle Q_{\text{i,eff}}/Q_{\text{i}} \rangle$  ranges from 0.22 to 0.50, while the time-averaged shielding factor  $\langle q \rangle = \langle Q_{\text{i,eff}}/\dot{N}_e \rangle$  ranges from 61 to 2950 (Table 2). Although dense, compact clouds tend to have a high hydrogen absorption fraction, they have a high shielding factor and hence inefficient photoevaporative mass loss. Assuming that the area of the IFs and thickness of the shielding layer scale with the dimensions of the initial cloud, we derive and calibrate expressions for the photoevaporation rate (Equations (11), (13); Figure 11a).

## 5. Outflow acceleration and properties

We perform a detailed analysis of the momentum injection processes that are responsible for cloud disruption and mass loss. The total radial momentum yield (momentum per stellar mass formed) of outflowing gas ranges over  $\sim 20\text{--}400 \text{ km s}^{-1}$  (Figure 12), scaling as  $p_*/m_* \propto \Sigma_0^{-0.74}$  (Equation (18)). The time-averaged total radial gas pressure force is smaller than the dustless, spherical case by a factor of  $\sim 5\text{--}10$  due to momentum cancellation and escape of radiation, but is within 30% of  $\dot{M}_{\text{ion}}c_i$ , where  $\dot{M}_{\text{ion}}$  and  $c_i$  refer to the mass evaporation rate and the sound speed of the ionized gas, respectively (Figure 13). This is consistent with expectations for both internal pressure forces within the ionized medium and the combined thermal pressure and recoil forces on neutral gas at IFs, both of which scale as  $n_i c_i^2 A_i \sim \dot{M}_{\text{ion}}c_i$ . Similarly, the time-averaged radial force from radiation pressure is much reduced below the naive spherical expectation to  $\sim 0.08\text{--}0.27 L/c$  because of flux cancellation and photon escape. Although the overall momentum injection by radiation feedback is less efficient in realistic turbulent clouds than suggested by analytic predictions based on spherical H II region expansion in smooth clouds (e.g. Krumholz & Matzner 2009; Murray et al. 2010; Fall et al. 2010; Kim et al. 2016), the ratio of radiation pressure forces to gas pressure forces increases for massive, high surface density clouds (Figure 14), consistent with expectations from these previous studies. The mean outflow velocity of ionized gas is mildly supersonic with  $v_{\text{ej,ion}} \sim 18\text{--}36 \text{ km s}^{-1}$ , while that of neutral gas is  $v_{\text{ej,neu}} \sim 6\text{--}15 \text{ km s}^{-1}$ , at about 0.8–1.8 times the escape velocity of the initial cloud (Figure 9 and Table 2).

## 6. Semi-analytic models

Based on our analyses of mass loss processes, we develop simple semi-analytic models for the net SFE,  $\varepsilon_*$ , and photoevaporation efficiency,  $\varepsilon_{\text{ion}}$ , as limited by radiation feedback in cluster-forming clouds. The predicted  $\varepsilon_{\text{ion}}$  is proportional to  $\varepsilon_*^{1/2} \Sigma_0^{-1}$  (Equation (26)), with an order-unity dimensionless coefficient  $\phi_t \phi_{\text{ion}}$  that we calibrate from simulations (Equation (16), Figure 11). When photoevaporation is the primary agent of cloud destruction, the net SFE depends solely on the gas surface density (Equation (29)). The resulting predictions for  $\varepsilon_*$  and  $\varepsilon_{\text{ion}}$  agree well with the numerical results for massive ( $\geq 10^5 M_\odot$ ) clouds (Figure 6(a) and (c)). In low-mass clouds ( $10^4 M_\odot$ ), the back-reaction to ionized-gas pressure is effective at IFs, and these clouds lose 30–50% of their initial gas mass as neutrals. Allowing for both ionized and neutral gas in outflows and assuming that the ejection velocity is constant for fixed cloud mass, with total momentum injection calibrated from our simulations (Equation (18)), the predicted net SFE (Equation (31)) has a weak dependence on the cloud mass, consistent with our numerical results (Figure 6).



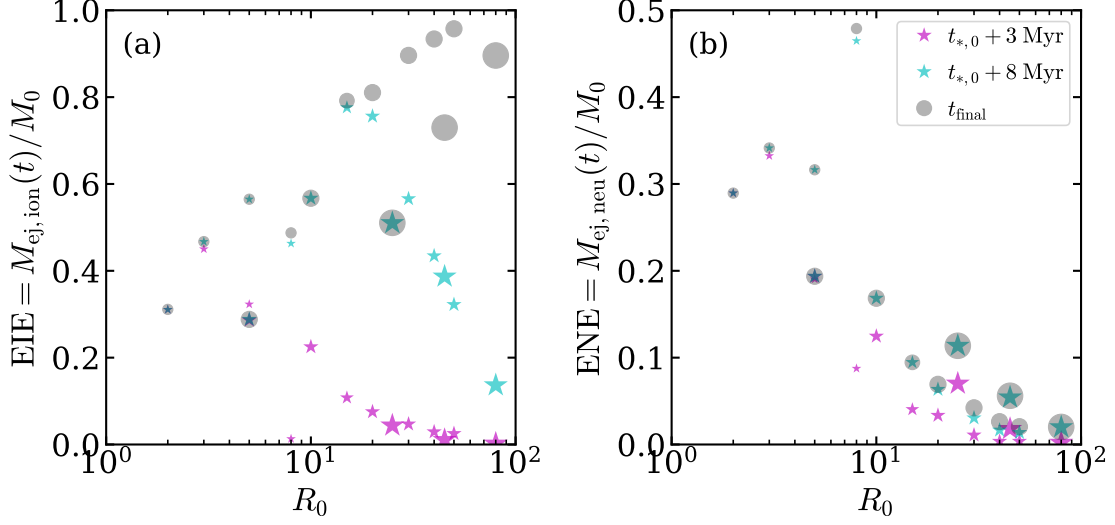


FIG. 15.— (a) Ejected ion efficiency (EIE) and (b) ejected neutral efficiency (ENE) at times  $t_{*,0} + t_{\text{SN}}$  (magenta),  $t_{*,0} + t_{\text{UV}}$  (cyan), and  $t_{\text{final}}$  (gray) as functions of the initial cloud radius  $R_0$ .

### 6.2. Discussion

It is interesting to compare our results with those of previous theoretical studies on star-forming GMCs with UV radiation feedback. Our net SFE and relative role of photoionization to radiation pressure are in qualitative agreement with the predictions of Kim et al. (2016), which adopted the idealizations of instantaneous star formation and spherical shell expansion (see also Fall et al. 2010; Murray et al. 2010; Rahner et al. 2017). However, the minimum SFE required for cloud disruption by ionized-gas pressure found by Kim et al. (2016) ( $\sim 0.002$ – $0.1$  for  $20 M_{\odot} \text{ pc}^{-2} \leq \Sigma_0 \leq 10^2 M_{\odot} \text{ pc}^{-2}$ , see their Figure 11) is smaller than what we find here. Turbulence-induced structure can lead to higher SFE for several reasons. First, a fraction of the photons can easily escape through low-density channels, without either ionizing gas or being absorbed to impart momentum. Second, low-density but high pressure ionized gas can also vent through these channels, reducing the transfer of momentum from photoevaporated to neutral gas. Third, turbulence increases the mass-weighted mean density and therefore the recombination rate of ionized gas, so that a higher luminosity is required to photoevaporate gas.

In this paper, we also find that radiation pressure becomes significant at  $\Sigma_0 \sim 200$ – $800 M_{\odot} \text{ pc}^{-2}$ , lower for higher-mass clouds. This transition value of surface density for low-mass clouds is somewhat higher than  $\Sigma_0 \sim 100 M_{\odot} \text{ pc}^{-2}$  in simple spherical models (e.g. Krumholz & Matzner 2009; Murray et al. 2010; Fall et al. 2010; Kim et al. 2016). These spherical models predicted that the expansion of an H II region is dominated by radiation pressure force at least in the early phase of expansion (e.g., Krumholz & Matzner 2009; Kim et al. 2016). Even for the highest- $\Sigma_0$  models, however, we find that the volume-integrated radiation pressure force ( $\int \mathbf{f}_{\text{rad}} \cdot \hat{\mathbf{r}} dV$ ) in the radial direction tends to be smaller than that of gas pressure force ( $\int \mathbf{f}_{\text{thm}} \cdot \hat{\mathbf{r}} dV$ ) in the early phase of star formation, and that this tendency is reversed only at late time. This is due to the strong cancellation of radiation on a global scale, and should thus not be inter-

preted as evidence for radiation pressure being subdominant. Rather, radiation pressure plays a greater role in controlling the dynamics of sub H II regions surrounding individual sources.

The outflow momentum yield of  $p_*/m_* \sim 20$ – $400 \text{ km s}^{-1}$  by radiation feedback found from our simulations can be compared with those produced by other types of feedback. For example, the momentum yield of protostellar outflows is estimated as  $\sim 40 \text{ km s}^{-1}$  (e.g., Matzner & McKee 2000), while recent numerical work on SNe-driven flows found a momentum yield of  $\sim 1000$ – $3000 \text{ km s}^{-1}$ , weakly dependent on the background density and stellar clustering (e.g., Kim & Ostriker 2015; Kim et al. 2017). These feedback mechanisms are expected to be important at different scales (e.g., Fall et al. 2010; Krumholz et al. 2014; Matzner & Jumper 2015). The momentum injection by protostellar outflows plays a key role in driving turbulence and regulating star formation in small-scale clumps before massive stars form (e.g., Nakamura & Li 2014), and SNe are capable of driving ISM turbulence to regulate galaxy-wide star formation and possibly winds from low-mass galaxies (e.g., Kim et al. 2017). Momentum injection by UV radiation is important to controlling dynamics at intermediate, GMC scales.

In this paper we have focused exclusively on the effects of radiation feedback, and as we neglect aging of stellar populations over the whole cloud lifetime, our mass-loss efficiencies place an upper limit to the actual damage UV radiation can cause. To estimate lower limits to the destructive effects of radiation feedback, we can consider what UV feedback would be able to accomplish over two shorter intervals:  $t_{\text{SN}} = 3 \text{ Myr}$ , the minimum lifetime of most massive stars (i.e., the time when first supernova is expected to occur after the epoch of the first star formation); and  $t_{\text{UV}} = 8 \text{ Myr}$ , the time scale on which UV luminosity decays. Figure 15 shows the cumulative (a) ejected ion efficiency  $\text{EIE} = M_{\text{ej,ion}}/M_0$  and (b) ejected neutral efficiency  $\text{ENE} = M_{\text{ej,neu}}/M_0$  as functions of the initial cloud radius  $R_0$  at  $t_{*,0} + t_{\text{SN}}$  (magenta),  $t_{*,0} + t_{\text{UV}}$

(cyan), and  $t_{\text{final}}$  (gray). In the case of compact, high-surface density clouds with short freefall times, the mass-loss efficiencies at  $t_{*,0} + t_{\text{SN}}$  are close to the final values at  $t_{\text{final}}$ , suggesting that UV radiation is expected to clear out most of gas prior to the first supernova. For large, diffuse clouds with long freefall times, the mass ejection efficiencies at  $t_{*,0} + t_{\text{SN}}$  and  $t_{*,0} + t_{\text{UV}}$  are significantly smaller than the final values. For these diffuse clouds with long freefall timescales, a complete assessment of star formation efficiency and cloud destruction will have to include the effects of supernovae as well as radiation feedback. While some of the supernova energy escapes easily through low-density channels (e.g. Rogers & Pittard 2013; Walch & Naab 2015), and supernovae may undermine radiation feedback by compressing overdense structures, supernova feedback likely aids in destroying star-forming clouds overall (e.g. Geen et al. 2016). In principle, shocked stellar winds may also be important over the same period as radiation feedback is active, although recent studies have raised doubts about its effectiveness as this hot gas can easily leak through holes or mix with cool gas (Harper-Clark & Murray 2009; Rosen et al. 2014).

In this work, we have considered only unmagnetized, marginally bound clouds with  $\alpha_{\text{vir},0} = 2$ , while observed GMCs may have a range of virial values (e.g., Heyer et al. 2009; Roman-Duval et al. 2010; Miville-Deschênes et al. 2017). Preliminary simulations we have done reveal that the net SFE decreases from 0.31 to 0.02 as  $\alpha_{\text{vir},0}$  is varied from 0.5 to 5 for the fiducial mass and size. Clouds with large initial  $\alpha_{\text{vir},0}$  tend to form stars less efficiently since turbulence unbinds a larger fraction of gas and reduces the gas mass in collapsing structures, as has been reported by recent simulations (e.g., Dale et al. 2013; Bertram et al. 2015; Howard et al. 2016; Raskutti et al. 2016; Dale 2017). For clouds that are initially strongly-bound, an initial adjustment period leads to smaller cloud with order-unity  $\alpha$ , in which the subsequent evolution is similar to clouds with  $\alpha_{\text{vir},0} \sim 1$  (Raskutti et al. 2016). Magnetization is likely to increase the effectiveness of radiation feedback, as it reduces the density inhomogeneity that limits radiation pressure effects, and may also help to distribute energy into neutral gas (Gendeleev & Krumholz 2012).

Finally, we comment on the resolution of our numerical models. Our standard choice of grid resolution ( $N_{\text{cell}} = 256^3$ ) and domain size ( $L_{\text{box}} = 4R_0$ ) is a compromise between computational time and accuracy, and this choice of moderate resolution enabled us to extensively explore parameter space. While the present simulations can capture the dynamics of cluster-forming gas and outflowing gas on cloud scales with reasonable accuracy, they do not properly resolve compressible flows in high-density regions where sink particles are created. Our models may overestimate star formation rates as all the gas that has been accreted onto sink particles is assumed to be converted to stars (cf. Howard et al. 2016, 2017), although a converging trend of  $\varepsilon_*$  with resolution (see Appendix A) suggests that the final SFE may be primarily controlled by photoevaporation and injection of momentum in moderate density gas at large scales. Adaptive mesh refinement simulations can be used to address this and other resolution-related questions.

We thank the anonymous referee for constructive comments on the manuscript. J.-G.K. would like to thank Michael Grudić, Takashi Hosokawa, Ralph Pudritz, and Benny Tsang for stimulating discussions. J.-G.K. acknowledges financial support from the National Research Foundation of Korea (NRF) through the grant NRF-2014-Fostering Core Leaders of the Future Basic Science Program. The work of W.-T.K. was supported by the National Research Foundation of Korea (NRF) grant funded by the Korean government (MEST) (No. 3348-20160021). The work of E.C.O. was supported by grant AST-1713949 from the U.S. National Science Foundation. The computation of this work was supported by the Supercomputing Center/Korea Institute of Science and Technology Information with supercomputing resources including technical support (KSC-2017-C3-0029), and the PICSiE TIGRESS High Performance Computing Center at Princeton University.

*Software:* Athena (Stone et al. 2008), yt (Turk et al. 2011), numpy (van der Walt et al. 2011), matplotlib (Hunter 2007), IPython (Pérez & Granger 2007), pandas (McKinney 2010), ParaView (Ayachit 2015).

## APPENDIX

### RESOLUTION STUDY OF THE FIDUCIAL MODEL

The high computational cost required for radiation transfer, especially for models involving numerous point sources, prevents us from running all our simulations at very high resolution. To study how our numerical results depend on the grid size, we run the fiducial model with  $M_0 = 10^5 M_\odot$  and  $R_0 = 20$  pc at three different spatial resolutions with  $N_{\text{cell}} = 128^3$  (M1E5R20\_N128),  $256^3$  (M1E5R20), and  $512^3$  (M1E5R20\_N512). Here we compare the results of these models.

Figure 16 plots the temporal evolution of various volume- or surface-integrated quantities from M1E5R20\_N128 (short dashed), M1E5R20 (solid), M1E5R20\_N512 (long dashed). It is clear that all quantities exhibit qualitatively similar behavior with time, and the final values of key quantities such as stellar mass and photoevaporated gas mass listed in Table 2 are numerically quite close and follow a converging trend as the resolution increases. For example, the increment in the duration of star formation  $t_{\text{SF}}$  from the  $128^3$  to  $256^3$  runs is  $\sim 25\%$ , which is reduced to  $\sim 17\%$  from the  $256^3$  to  $512^3$  runs. This resolution-dependent  $t_{\text{SF}}$  is due primarily to the fact that the minimum sink particle mass as well as the physical size of the control volume (or the effective area through which gas accretes) are proportional to  $\Delta x$  (or  $\Delta x^2$ ), so that the stellar mass grows more rapidly and in a more discrete fashion at coarser spatial resolution. Despite this difference, the net SFE of 0.15, 0.13, and 0.12 for  $N_{\text{cell}} = 128^3$ ,  $256^3$ , and  $512^3$ , respectively, is almost converged.

Figure 17 compares sample snapshots of the total (neutral + ionized) gas surface density and the emission measure projected along the  $z$ -axis when 80% of the final stellar mass has been formed (at  $t/t_{\text{ff},0} = 1.10, 1.31, 1.45$  for  $N_{\text{cell}} = 128^3$ ,  $256^3$ , and  $512^3$ , respectively). The higher-resolution model exhibits filaments, pillars, and bright-rimmed globules in greater detail, but the overall morphologies of gas and star particle distributions are very

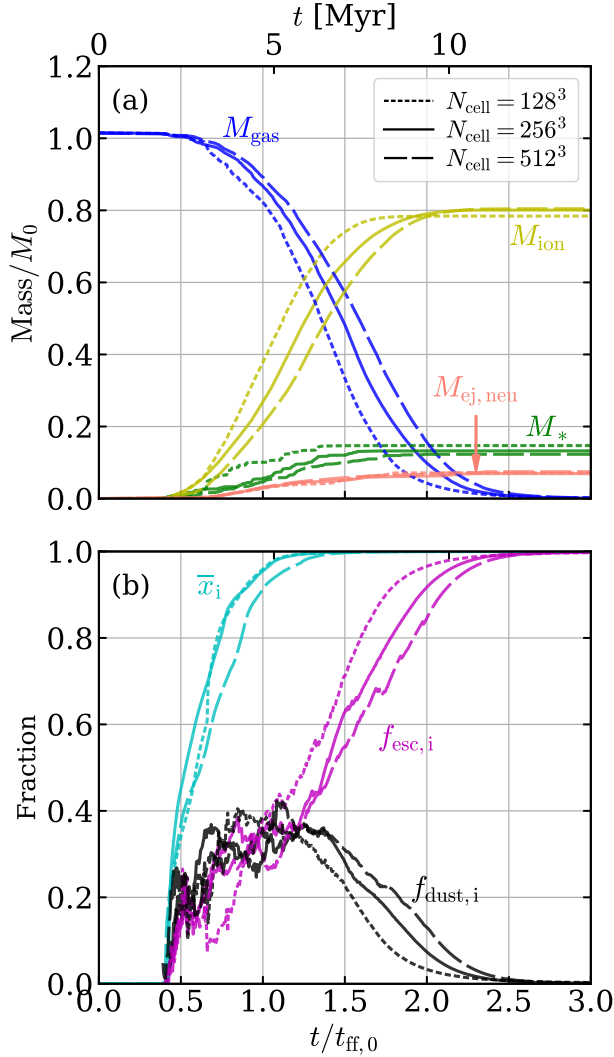


FIG. 16.— Evolutionary histories of key quantities for the fiducial cloud model ( $M_0 = 10^5 M_\odot$  and  $R_0 = 20$  pc) at varying resolution:  $N_{\text{cell}} = 128^3$  (short dashed),  $256^3$  (solid), and  $512^3$  (long dashed). (a) The total gas mass  $M_{\text{gas}}$  in the simulation volume (blue), the stellar mass  $M_*$  (green), the ejected neutral gas mass  $M_{\text{ej,neu}}$  (salmon), and the mass of the photoevaporated gas  $M_{\text{ion}}$  (yellow). (b) The volume fraction of the ionized gas  $\bar{x}_i$  (cyan), the fraction of ionizing radiation absorbed by dust  $f_{\text{dust},i}$  (black), and the escape fractions of ionizing photons  $f_{\text{esc},i}$  (magenta).

similar. Therefore, we conclude that the results based on  $N_{\text{cell}} = 256^3$  presented in the paper provide quantitatively reasonable estimates to the converged results.

#### NET STAR FORMATION EFFICIENCY REGULATED BY RADIATION-PRESSURE FEEDBACK

Here we compare the net SFE from our RP-only simulations with the analytic predictions by Raskutti et al. (2016) and Thompson & Krumholz (2016). The key underlying assumptions of these models are that (1) the probability density function (PDF) of gas surface density follows a log-normal distribution, characteristic of supersonic isothermal turbulence and that (2) only the gas with surface density below the Eddington surface density is ejected. These analytic models predict a higher SFE for a turbulent cloud than for an equivalent uni-

form cloud (e.g., Fall et al. 2010; Kim et al. 2016) with the same mass and size because a greater luminosity is required to eject gas compressed to high surface density by turbulence.

Raskutti et al. (2016) argued that for a cloud with given log-normal variance in the surface density  $\sigma_{\ln \Sigma^c}$ , the luminosity would continue to rise until it reaches a level that maximizes the outflow efficiency. At this point, the final SFE would be bracketed between two levels,  $\varepsilon_{*,\text{min}}$  and  $\varepsilon_{*,\text{max}}$ . At one extreme, all the remaining gas can be ejected without forming stars, if the PDF adjusts itself rapidly to a successively lower peak as gas is expelled. At the opposite extreme, all of the remaining gas can turn into stars if it collapses before the PDF adjusts. Thompson & Krumholz (2016) considered a similar situation, but they allowed for a time-dependent star formation rate  $\dot{M}_* = \varepsilon_{\text{ff}} M_{\text{gas}}(t)/t_{\text{ff}}$ , where  $\varepsilon_{\text{ff}}$  is a free parameter. In both models, gas is assumed to be ejected rapidly.

In our simulations, the gas column density distribution remains broad over the entire evolution. The column density PDFs closely resemble log-normal functions with  $\sigma_{\ln \Sigma^c} \sim 1.2$ – $1.6$  that do not vary much over the star-forming period (from  $t_{*,10\%}$  to  $t_{*,90\%}$ ), roughly consistent with the results of Raskutti et al. (2016). The effective SFE per freefall time  $\varepsilon_{\text{ff,eff}} = \varepsilon_* t_{\text{ff},0}/(t_{*,99\%} - t_{*,0})$  in each model turns out to vary in the range of 0.1–0.22 across our models. Both analytic models in principle allow for the cloud size to vary over time, although the numerical simulations of Raskutti et al. (2016) show that the effective radius in fact varies very little up until the cloud is rapidly dispersed. Here, to compare to the analytic models, we assume the cloud size is fixed at its initial radius ( $x = 1$  in Raskutti et al. 2016 and  $p = 0$  in Thompson & Krumholz 2016), and we take a fixed value  $\sigma_{\ln \Sigma^c} = 1.4$ .

Figure 18 compares the net SFE resulting from our RP-only runs (squares) with the theoretical predictions (various lines). For this purpose, we adjust the numerical results, i.e.,  $\varepsilon_{*,\text{adj}} = \varepsilon_*/(1 - \varepsilon_{\text{ej,turb}})$ , to allow for initial turbulent outflow, similar to Raskutti et al. (2016). The numerical results lie between  $\varepsilon_{*,\text{min}}$  and  $\varepsilon_{*,\text{max}}$  (black solid lines) predicted by Raskutti et al. (2016). The net SFE is to some extent closer to  $\varepsilon_{*,\text{min}}$  than  $\varepsilon_{*,\text{max}}$ , which is in contrast to the numerical results of Raskutti et al. (2016) (see their Figure 25). In Paper I, we previously showed that the net SFE obtained using the  $M_1$ -closure as in Raskutti et al. (2016) is higher than that obtained from the adaptive ray tracing method, because in the former the source function is smoothed out over a finite region and thus the radiation force in the immediate vicinity of star particles is lower than it should be, allowing additional accretion of nearby gas.

Figure 18 plots as a dotted lines the net SFE predicted by the Thompson & Krumholz formalism, adopting  $\varepsilon_{\text{ff}} = 0.1$  and 0.2 to bracket our simulation results (note that they adopted a much lower value for their fiducial model). The prediction brackets the results of our simulations.

We conclude that the results of our RP-only simulations are overall in good agreement with the recent analytic models of Raskutti et al. (2016) and Thompson & Krumholz (2016) for the net SFE in turbulent star-forming clouds regulated by radiation pressure.

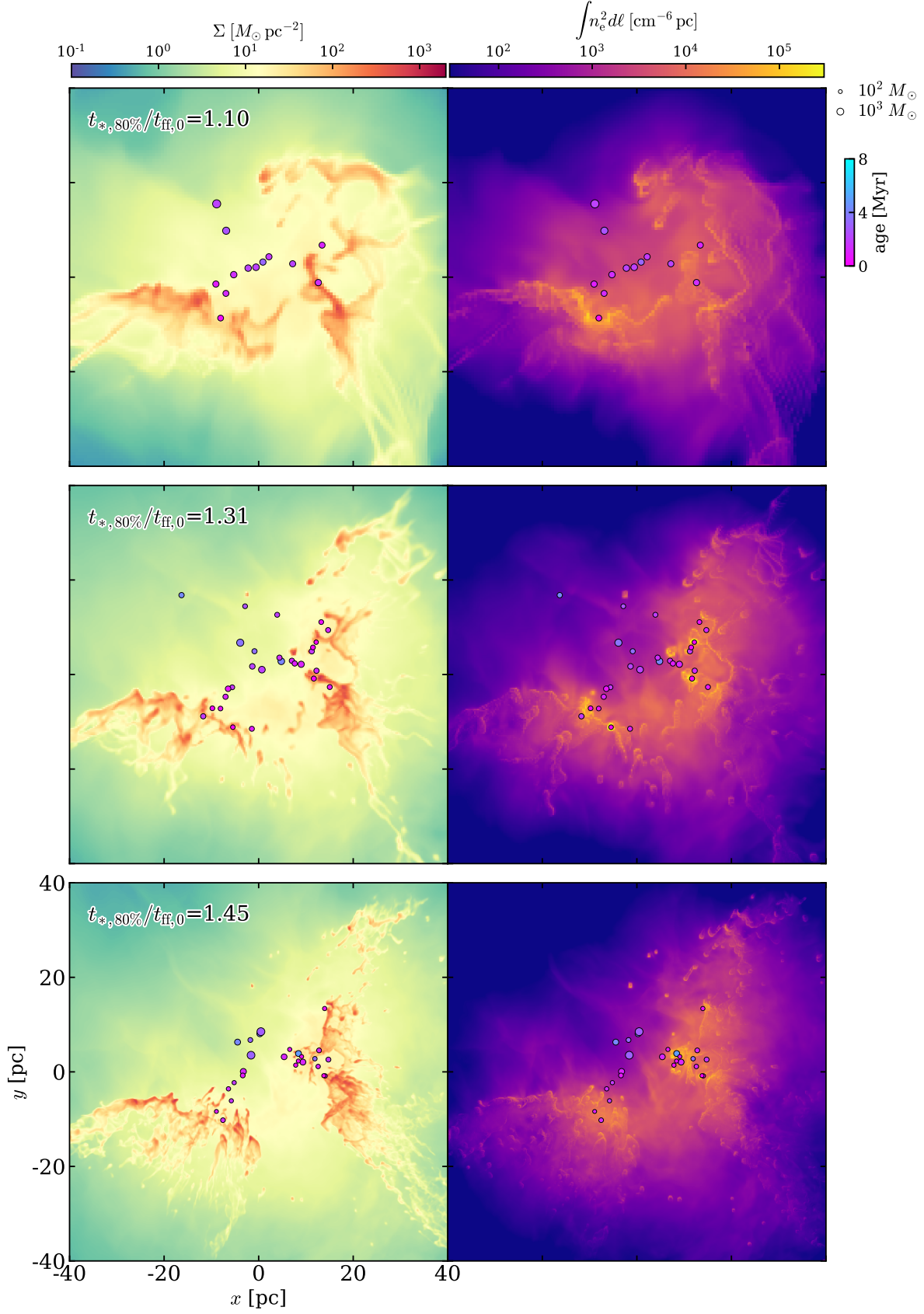


FIG. 17.— Snapshots of the gas surface density (left) and emission measure (right) in the fiducial model when 80% of the final stellar mass has been assembled. The top, middle, and bottom panels correspond respectively to the run with  $N_{\text{cell}} = 128^3$  at  $t/t_{\text{ff},0} = 1.10$ ,  $256^3$  at  $t/t_{\text{ff},0} = 1.31$ , and  $512^3$  at  $t/t_{\text{ff},0} = 1.45$ . The projected positions of star particles are shown as circles, with their color corresponding to age.



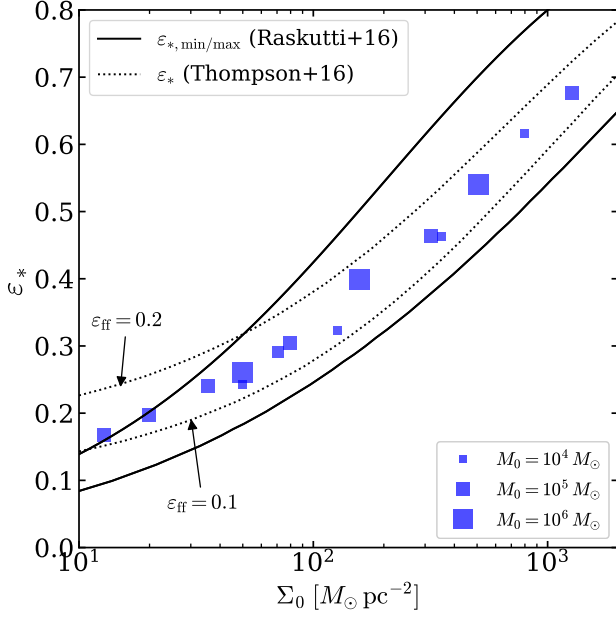


FIG. 18.— Comparison of the net SFE from the RP-only simulations (squares) with those from the theoretical predictions (lines). The solid lines show  $\varepsilon_{*,\min}$  and  $\varepsilon_{*,\max}$  based on the analytic model of Raskutti et al. (2016). The predictions of Thompson & Krumholz (2016) with  $\varepsilon_{\text{ff}} = 0.1, 0.2$  are given as dotted lines. For both models we adopt  $\sigma_{\text{In } \Sigma^c} = 1.4$  based on the typical variance in our simulations.

## REFERENCES

- Abel, T., & Wandelt, B. D. 2002, MNRAS, 330, L53 [1, 2.1]  
 Ayachit, U. 2015, The Paraview Guide: A Parallel Visualization Application, Kitware, Inc., USA, 2015 [6.2]  
 Baczynski, C. 2015, PhD thesis, Universität Heidelberg [2.1]  
 Baczynski, C., Glover, S. C. O., & Klessen, R. S. 2015, MNRAS, 454, 380 [2]  
 Ballesteros-Paredes, J. 2006, MNRAS, 372, 443 [1]  
 Ballesteros-Paredes, J., Hartmann, L. W., Vázquez-Semadeni, E., Heitsch, F., & Zamora-Avilés, M. A. 2011, MNRAS, 411, 65 [1]  
 Bertoldi, F. 1989, ApJ, 346, 735 [1, 4.1.1, 4.1.1]  
 Bertoldi, F., & McKee, C. F. 1990, ApJ, 354, 529 [3.4]  
 Bertram, E., Glover, S. C. O., Clark, P. C., & Klessen, R. S. 2015, MNRAS, 451, 3679 [6.2]  
 Bigiel, F., Leroy, A., Walter, F., et al. 2008, AJ, 136, 2846 [1]  
 Bisbas, T. G., Wunsch, R., Whitworth, A. P., Hubber, D. A., & Walch, S. 2011, ApJ, 736, 142 [1]  
 Blitz, L., Fukui, Y., Kawamura, A., et al. 2007, Protostars and Planets V, 81 [1]  
 Carpenter, J. M. 2000, AJ, 120, 3139 [1]  
 Colín, P., Vázquez-Semadeni, E., & Gómez, G. C. 2013, MNRAS, 435, 1701 [1]  
 Colombo, D., Hughes, A., Schinnerer, E., et al. 2014, ApJ, 784, 3 [1]  
 Consiglio, S. M., Turner, J. L., Beck, S., & Meier, D. S. 2016, ApJ, 833, L6 [1]  
 Daddi, E., Elbaz, D., Walter, F., et al. 2010, ApJ, 714, L118 [1]  
 Dale, J. E. 2015, New A Rev., 68, 1 [1]  
 —. 2017, MNRAS, 467, 1067 [4.2.2, 6.2]  
 Dale, J. E., Bonnell, I. A., & Whitworth, A. P. 2007, MNRAS, 375, 1291 [1]  
 Dale, J. E., Ercolano, B., & Bonnell, I. A. 2012, MNRAS, 424, 377 [1, 4, 3.2, 4.1.1]  
 —. 2013, MNRAS, 430, 234 [1, 6.2]  
 Da Rio, N., Tan, J. C., & Jaehnig, K. 2014, ApJ, 795, 55 [1]  
 Deharveng, L., Schuller, F., Anderson, L. D., et al. 2010, A&A, 523, A6 [1]  
 Draine, B. T. 2011, ApJ, 732, 100 [1, 2.1, 4.2.2]  
 Elmegreen, B. G. 2000, ApJ, 530, 277 [1, 3.3]  
 Elmegreen, B. G., & Lada, C. J. 1977, ApJ, 214, 725 [1]  
 Elmegreen, B. G., & Scalo, J. 2004, ARA&A, 42, 211 [1]  
 Elmegreen, B. G. 1976, ApJ, 205, 405 [4.1.1]  
 Engargiola, G., Plambeck, R. L., Rosolowsky, E., & Blitz, L. 2003, ApJS, 149, 343 [1]  
 Evans, II, N. J. 1991, in Astronomical Society of the Pacific Conference Series, Vol. 20, Frontiers of Stellar Evolution, ed. D. L. Lambert, 45–95 [1]  
 Evans, II, N. J., Dunham, M. M., Jørgensen, J. K., et al. 2009, ApJS, 181, 321 [1]  
 Fall, S. M., Krumholz, M. R., & Matzner, C. D. 2010, ApJ, 710, L142 [1, 4.2.2, 5, 6.2, B]  
 García, P., Bronfman, L., Nyman, L.-Å., Dame, T. M., & Luna, A. 2014, ApJS, 212, 2 [1]  
 Gavagnin, E., Bleuler, A., Rosdahl, J., & Teyssier, R. 2017, MNRAS, 472, 4155 [1]  
 Geen, S., Hennebelle, P., Tremblin, P., & Rosdahl, J. 2016, MNRAS, 463, 3129 [6.2]  
 Geen, S., Soler, J. D., & Hennebelle, P. 2017, MNRAS, 471, 4844 [1]  
 Gendele, L., & Krumholz, M. R. 2012, ApJ, 745, 158 [6.2]  
 Goldbaum, N. J., Krumholz, M. R., Matzner, C. D., & McKee, C. F. 2011, ApJ, 738, 101 [1]  
 Gong, H., & Ostriker, E. C. 2013, ApJS, 204, 8 [2.1]  
 Górski, K. M., Hivon, E., Banday, A. J., et al. 2005, ApJ, 622, 759 [2.1]  
 Gritschneider, M., Burkert, A., Naab, T., & Walch, S. 2010, ApJ, 723, 971 [3.1]  
 Gritschneider, M., Naab, T., Walch, S., Burkert, A., & Heitsch, F. 2009, ApJ, 694, L26 [1, 3.1]  
 Harper-Clark, E., & Murray, N. 2009, ApJ, 693, 1696 [6.2]  
 Hartigan, P., Reiter, M., Smith, N., & Bally, J. 2015, AJ, 149, 101 [3.1]  
 Hartmann, L. 2001, AJ, 121, 1030 [1]  
 Hartmann, L., Ballesteros-Paredes, J., & Bergin, E. A. 2001, ApJ, 562, 852 [1]  
 Heyer, M., & Dame, T. M. 2015, ARA&A, 53, 583 [1, 3.3]  
 Heyer, M., Krawczyk, C., Duval, J., & Jackson, J. M. 2009, ApJ, 699, 1092 [1, 6.2]

- Hockney, R. W., & Eastwood, J. W. 1981, *Computer Simulation Using Particles* [2.1]
- Hopkins, P. F., & Grudić, M. Y. 2018, arXiv:1803.07573 [2.1]
- Hosokawa, T., & Inutsuka, S.-i. 2006, *ApJ*, 646, 240 [1]
- Howard, C. S., Pudritz, R. E., & Harris, W. E. 2016, *MNRAS*, 461, 2953 [6.2]
- . 2017, *MNRAS*, 470, 3346 [1, 6.2]
- Hunter, J. D. 2007, *CSE*, 9, 90 [6.2]
- Kahn, F. D. 1969, *Physica*, 41, 172 [4.1.1]
- Kawamura, A., Mizuno, Y., Minamidani, T., et al. 2009, *ApJS*, 184, 1 [1]
- Kennicutt, R. C., & Evans, N. J. 2012, *ARA&A*, 50, 531 [1]
- Kim, C.-G., & Ostriker, E. C. 2015, *ApJ*, 802, 99 [4.2.1, 6.2]
- Kim, C.-G., Ostriker, E. C., & Kim, W.-T. 2013, *ApJ*, 776, 1 [4.2.1]
- Kim, C.-G., Ostriker, E. C., & Raileanu, R. 2017, *ApJ*, 834, 25 [4.2.1, 6.2]
- Kim, J.-G., & Kim, W.-T. 2014, *ApJ*, 797, 135 [2.1]
- Kim, J.-G., Kim, W.-T., & Ostriker, E. C. 2016, *ApJ*, 819, 137 [1, 2.1, 4.2.2, 4.2.2, 5.2, 5, 6.2, B]
- Kim, J.-G., Kim, W.-T., Ostriker, E. C., & Skinner, M. A. 2017, *ApJ*, 851, 93 (Paper I) [1, 2, 2.1, 3.2, B]
- Koenig, X. P., Leisawitz, D. T., Benford, D. J., et al. 2012, *ApJ*, 744, 130 [3.1]
- Krumholz, M. R., & Matzner, C. D. 2009, *ApJ*, 703, 1352 [1, 4.2.2, 4.2.2, 5, 6.2]
- Krumholz, M. R., Matzner, C. D., & McKee, C. F. 2006, *ApJ*, 653, 361 [1, 4.2.2]
- Krumholz, M. R., Stone, J. M., & Gardiner, T. A. 2007, *ApJ*, 671, 518 [2.1]
- Krumholz, M. R., Bate, M. R., Arce, H. G., et al. 2014, *Protostars and Planets VI*, 243 [1, 6.2]
- Lee, E. J., Miville-Deschênes, M.-A., & Murray, N. W. 2016, *ApJ*, 833, 229 [1]
- Lefloch, B., & Lazareff, B. 1994, *A&A*, 289, 559 [1]
- Leroy, A. K., Walter, F., Sandstrom, K., et al. 2013, *AJ*, 146, 19 [1]
- Leroy, A. K., Bolatto, A. D., Ostriker, E. C., et al. 2015, *ApJ*, 801, 25 [1]
- Mac Low, M.-M., Klessen, R. S., Burkert, A., & Smith, M. D. 1998, *Physical Review Letters*, 80, 2754 [1]
- Matzner, C. D. 2002, *ApJ*, 566, 302 [1, 4.2.2]
- Matzner, C. D., & Jumper, P. H. 2015, *ApJ*, 815, 68 [6.2]
- Matzner, C. D., & McKee, C. F. 2000, *ApJ*, 545, 364 [6.2]
- McKee, C. F., & Ostriker, E. C. 2007, *ARA&A*, 45, 565 [1]
- McKinney, W. 2010, in *Proc. 9th Python in Science Conf., Data Structures for Statistical Computing in Python*, ed. S. van der Walt & J. Millman (Austin, TX: SciPy), 51 [6.2]
- Medina, S.-N. X., Arthur, S. J., Henney, W. J., Mellema, G., & Gazol, A. 2014, *MNRAS*, 445, 1797 [1]
- Meidt, S. E., Hughes, A., Dobbs, C. L., et al. 2015, *ApJ*, 806, 72 [1]
- Meier, D. S., Turner, J. L., & Beck, S. C. 2002, *AJ*, 124, 877 [1]
- Mellema, G., Arthur, S. J., Henney, W. J., Iliev, I. T., & Shapiro, P. R. 2006, *ApJ*, 647, 397 [3.1]
- Miura, R. E., Kohno, K., Tosaki, T., et al. 2012, *ApJ*, 761, 37 [1]
- Miville-Deschênes, M.-A., Murray, N., & Lee, E. J. 2017, *ApJ*, 834, 57 [6.2]
- Mooney, T. J., & Solomon, P. M. 1988, *ApJ*, 334, L51 [1]
- Murray, N. 2011, *ApJ*, 729, 133 [1]
- Murray, N., Quataert, E., & Thompson, T. A. 2010, *ApJ*, 709, 191 [1, 4.2.2, 5, 6.2]
- Myers, P. C., Dame, T. M., Thaddeus, P., et al. 1986, *ApJ*, 301, 398 [1]
- Naab, T., & Ostriker, J. P. 2017, *ARA&A*, 55, 59 [4.2.1]
- Nakamura, F., & Li, Z.-Y. 2014, *ApJ*, 783, 115 [6.2]
- Oka, T., Hasegawa, T., Sato, F., et al. 2001, *ApJ*, 562, 348 [1]
- Oort, J. H., & Spitzer, Jr., L. 1955, *ApJ*, 121, 6 [4.1.1]
- Ostriker, E. C., & Shetty, R. 2011, *ApJ*, 731, 41 [4.2.1]
- Parravano, A., Hollenbach, D. J., & McKee, C. F. 2003, *ApJ*, 584, 797 [2.1]
- Pereira-Santaella, M., Colina, L., García-Burillo, S., et al. 2016, *A&A*, 587, A44 [1]
- Pérez, F., & Granger, B. E. 2007, *CSE*, 9, 21 [6.2]
- Peters, T., Banerjee, R., Klessen, R. S., et al. 2010, *ApJ*, 711, 1017 [4.1.1]
- Rahner, D., Pellegrini, E. W., Glover, S. C. O., & Klessen, R. S. 2017, *MNRAS*, 470, 4453 [1, 5.2, 6.2]
- Raskutti, S. 2016, PhD thesis, Princeton University []
- Raskutti, S., Ostriker, E. C., & Skinner, M. A. 2016, *ApJ*, 829, 130 [1, 2.2, 3.1, 3.2, 10, 6.2, B, 18]
- . 2017, *ApJ*, 850, 112 [1, 3.1, 4.2.2]
- Rogers, H., & Pittard, J. M. 2013, *MNRAS*, 431, 1337 [3.1, 6.2]
- Roman-Duval, J., Jackson, J. M., Heyer, M., Rathborne, J., & Simon, R. 2010, *ApJ*, 723, 492 [1, 6.2]
- Rosen, A. L., Krumholz, M. R., Oishi, J. S., Lee, A. T., & Klein, R. I. 2017, *JCoPh*, 330, 924 [1]
- Rosen, A. L., Lopez, L. A., Krumholz, M. R., & Ramirez-Ruiz, E. 2014, *MNRAS*, 442, 2701 [6.2]
- Skinner, M. A., & Ostriker, E. C. 2015, *ApJ*, 809, 187 [2.1, 2.2, 2.3]
- Stone, J. M., & Gardiner, T. 2009, *New A*, 14, 139 [1, 2.1]
- Stone, J. M., Gardiner, T. A., Teuben, P., Hawley, J. F., & Simon, J. B. 2008, *ApJS*, 178, 137 [2, 6.2]
- Stone, J. M., Ostriker, E. C., & Gammie, C. F. 1998, *ApJ*, 508, L99 [1]
- Sugitani, K., Fukui, Y., Mizuni, A., & Ohashi, N. 1989, *ApJ*, 342, L87 [1]
- Thompson, T. A., & Krumholz, M. R. 2016, *MNRAS*, 455, 334 [1, 3.2, B, 18]
- Tsang, T.-H. B., & Milosavljevic, M. 2017, *ArXiv e-prints*, arXiv:1709.07539 [2.3]
- Turk, M. J., Smith, B. D., Oishi, J. S., et al. 2011, *ApJS*, 192, 9 [6.2]
- Turner, J. L., Beck, S. C., Benford, D. J., et al. 2015, *Nature*, 519, 331 [1]
- Turner, J. L., Consiglio, S. M., Beck, S. C., et al. 2017, *ApJ*, 846, 73 [1]
- van der Walt, S., Colbert, S. C., & Varoquaux, G. 2011, *CSE*, 13, 22 [6.2]
- Vázquez-Semadeni, E., Colín, P., Gómez, G. C., Ballesteros-Paredes, J., & Watson, A. W. 2010, *ApJ*, 715, 1302 [1]
- Vutisalchavakul, N., Evans, II, N. J., & Heyer, M. 2016, *ApJ*, 831, 73 [1]
- Walch, S. K., Whitworth, A. P., Bisbas, T., Wünsch, R., & Hubber, D. 2012, *MNRAS*, 427, 625 [1, 3.1]
- Walch, S., & Naab, T. 2015, *MNRAS*, 451, 2757 [6.2]
- Whitworth, A. 1979, *MNRAS*, 186, 59 [1]
- Whitworth, A. P., Bhattal, A. S., Chapman, S. J., Disney, M. J., & Turner, J. A. 1994, *MNRAS*, 268, 291 [1]
- Williams, J. P., & McKee, C. F. 1997, *ApJ*, 476, 166 [1]
- Wilson, B. A., Dame, T. M., Masheder, M. R. W., & Thaddeus, P. 2005, *A&A*, 430, 523 [2.3]
- Wong, T., Hughes, A., Ott, J., et al. 2011, *ApJS*, 197, 16 [1]
- Zuckerman, B., & Evans, II, N. J. 1974, *ApJ*, 192, L149 [1]
- Zuckerman, B., & Palmer, P. 1974, *ARA&A*, 12, 279 [1]